

## A Triple-Moment Representation of Ice in the Predicted Particle Properties (P3) Microphysics Scheme

JASON A. MILBRANDT,<sup>a</sup> HUGH MORRISON,<sup>b,c</sup> DANIEL T. DAWSON II,<sup>d</sup> AND MARCO PAUKERT<sup>e,f</sup>

<sup>a</sup> Research Division, Environment and Climate Change Canada, Dorval, Quebec, Canada

<sup>b</sup> National Center for Atmospheric Research, Boulder, Colorado

<sup>c</sup> Australian Research Council Centre for Excellence in Climate System Science, University of New South Wales, Sydney, New South Wales, Australia

<sup>d</sup> Purdue University, West Lafayette, Indiana

<sup>e</sup> Pacific Northwest National Laboratory, Richland, Washington

(Manuscript received 16 March 2020, in final form 7 October 2020)

**ABSTRACT:** In the original Predicted Particle Properties (P3) bulk microphysics scheme, all ice-phase hydrometeors are represented by one or more “free” ice categories, where the physical properties evolve smoothly through changes to the four prognostic variables (per category), and with a two-moment representation of the particle size distribution. As such, the spectral dispersion cannot evolve independently, which thus results in limitations in representation of ice—in particular, hail—due to necessary constraints in the scheme to prevent excessive gravitational size sorting. To overcome this, P3 has been modified to include a three-moment representation of the size distribution of each ice category through the addition of a fifth prognostic variable, the sixth moment of the size distribution. The details of the three-moment ice parameterization in P3 are provided. The behavior of the modified scheme, with the single-ice-category configuration, is illustrated through simulations in a simple 1D kinematic model framework as well as with near large-eddy-resolving (250-m grid spacing) 3D simulations of a hail-producing supercell. It is shown that the three-moment ice configuration controls size sorting in a physically based way and leads to an improved capacity to simulate large, heavily rimed ice (hail), including mean and maximum sizes and reflectivity, and thus an overall improvement in the representation of ice-phase particles in the P3 scheme.

**KEYWORDS:** Cloud parameterizations; Cloud resolving models

### 1. Introduction

The techniques for representing frozen hydrometeors and parameterizing ice-phase processes in bulk microphysics schemes (BMSs) have advanced considerably. Originally, the inclusion of ice was done through the use of one or more single-moment categories that were considered to be representative of a particular type of particle (e.g., graupel), with the bulk properties (e.g., density) prescribed by constant parameters. Modern BMS are often very detailed, multimoment schemes with several ice-phase categories (e.g., Milbrandt and Yau 2005a; Seifert and Beheng 2006; Morrison et al. 2009; Lim and Hong 2010; Thompson and Eidhammer 2014; Chen and Tsai 2016). Over the last decade, the modeling community has seen a shift away from using an increasing number of prescribed ice-phase categories and toward emphasis on the addition of more predictive information but for a smaller number of categories in BMSs (e.g., Morrison and Grabowski 2008; Harrington et al. 2013; Sulia et al. 2014; Morrison and Milbrandt 2015, hereafter MM15; Chen and Tsai 2016; Jensen et al. 2017).

In the Predicted Particle Properties (P3) scheme, introduced in MM15 and Milbrandt and Morrison (2016), all ice-phase hydrometeors are represented by a user-specified number of “free” frozen categories, each of which can, in principle represent any type of ice-phase particle (within the limitations of a bulk scheme and specific constraints of P3) and whose physical properties evolved smoothly in time and space. It was shown in Morrison et al. (2015) that even with a single ice category, P3 performs well compared to detailed, state-of-the art, multicategory BMSs and can realistically simulate a wide range of ice-phase particles in deep convective and stratiform weather systems. The multicategory configuration overcomes the limitation that more than one dominant ice type (or mode) cannot coexist at the same time and location, thereby reducing the problems associated with dilution of particle properties due to mixing (physical or numerical). There are several advantages to the free-category approach, the most notable being the removal of the need for arbitrary and artificial “conversion” between categories, a necessary and inherently problematic aspect of traditional schemes.

Recent developments to P3 include the incorporation of a three-moment rain category (Paukert et al. 2019), the addition of a prognostic variable to predict the liquid fraction of an ice category thus allowing for mixed-phase particles (Chouette et al. 2019), and a diagnostic scheme for subgrid-scale clouds and precipitation based on Chouette et al. (2014). A merging of these various parallel developments into a single code version is currently underway (at the time of writing). The new

 Denotes content that is immediately available upon publication as open access.

<sup>f</sup> Deceased.

Corresponding author: Jason Milbrandt, jason.milbrandt@ec.gc.ca

developments described in this article, however, are built upon the original P3 version.

Despite its conceptual and practical advantages, P3 has limitations in terms of the flexibility of representing the particle size distribution (PSD) of ice-phase hydrometeors. Specifically, the shape parameter  $\mu$  (see section 2), which is a measure of the relative spectral dispersion of the PSD [given by (1); see below], varies monotonically with the slope parameter  $\lambda$  and thus cannot vary independently. A variable dispersion is important because it controls excessive size sorting, which is problematic in two-moment schemes (e.g., Wacker and Seifert 2000; Milbrandt and Yau 2005a; Mansell 2010). Furthermore, all of the process rates are affected directly by  $\mu$  (e.g., Milbrandt and Yau 2005a). The current diagnostic- $\mu$  relation in P3 is based on observations of unrimed or lightly rimed ice crystals and may not be appropriate for graupel and hail. As a result of this treatment of  $\mu$ , there is a need to constrain the ice PSD by imposing a fairly stringent maximum mean size (2 mm), primarily to control size sorting. This is equivalent to having a lower limit for  $\lambda$ . Consequently, the original P3 has a poor representation of hail in terms of sizes as well as simulated dual-polarity radar fields (Johnson et al. 2019). This may also mean degradation in the simulation of rimed ice in convective cores, which ultimately affects storm structure and evolution. Allowing the shape parameter of each ice category in P3 to vary freely would overcome these limitations.

For  $\mu$  to vary independently from the number and mean particle size, a BMS must predict at least three independent moments of the PSD. Although each ice category in P3 has 4 degrees of freedom for each population of ice (with four prognostic variables), there are only 2 degrees of freedom for the PSD given that there are only two independent moments of the distribution. Milbrandt and Yau (2005a,b; hereafter MY05a,b) examined the role of the shape parameter in detail and introduced a fully triple-moment bulk scheme. They showed that the three-moment approach improves several aspects of two-moment schemes, in particular for the treatment of hydrometeor sedimentation, where the problems associated with excessive size sorting are overcome through the independently varying shape parameter. The MY05 scheme was used to improve the simulation of hail in a simulated supercell (Milbrandt and Yau 2006a,b), for the further examination of tornadic supercells (Dawson et al. 2010, 2015, 2016), and has been applied to storm-scale data assimilation (e.g., Xue et al. 2010; Jung et al. 2012; Putnam et al. 2014, 2019; Dawson et al. 2015, 2016). Since the initial development and testing of the MY05 scheme, the three-moment approach has also been used to develop or advance other bulk schemes (e.g., Yang and Yau 2008; Shipway and Hill 2012; Dawson et al. 2014; Loftus et al. 2014; Chen and Tsai 2016).

Given the added value of the three-moment method, it is logical to apply this to ice in P3 in order to address some of the current limitations and to improve its capacity to simulate a wide range of ice-phase particles. To that end, we have adapted and applied the three-moment approach in P3 through the addition of a prognostic equation for the ice reflectivity factor. To our knowledge, this is the first attempt to treat a free (nonprescribed) ice category using the three-moment approach. The objectives of this article are 1) to describe and

document the modifications pertaining to the new three-moment representation of ice in P3; and 2) to illustrate the impacts and benefits of the modified scheme, in particular with respect to the simulation of hail. The modified version of P3 was used to perform quasi-idealized, cloud-resolving simulations of a nontornadic, hail-producing supercell, along with sensitivity experiments using two- and three-moment configurations.

The remainder of the article is organized as follows: section 2 provides a brief overview of the original P3 scheme along with details on the implementation of three-moment ice. In section 3, the behavior of the three-moment-ice version of P3 is illustrated in a simple context using a 1D kinematic cloud model. Section 4 describes the results of the idealized supercell simulations, with comparisons of results with two-moment and three-moment ice configurations. In section 5, discussion is provided regarding the importance of the specific prognostic triple-moment variable for advection, the feasibility of an improved diagnostic relation for the shape parameter for the two-moment configuration, and the effects on the results with coarser horizontal resolution. Concluding remarks are given in section 6.

## 2. Scheme description

### a. Overview of the original P3

The baseline version of the P3 scheme, used as the starting point for the development presented herein, is described in detail in MM15. In this study, only the one-ice-category configuration is used; results from the three-moment-ice parameterization with the multicategory configuration (Milbrandt and Morrison 2016) will be presented in a future study. The liquid-phase component of P3 has two-moment cloud droplet and rain categories. A brief overview of the treatment of the ice phase is provided here to facilitate the description of the changes made to the scheme. All symbols used in this paper are summarized in Table 1.

In general, all ice-phase hydrometeors in the original P3 are represented by a user-specified number of free ice categories ( $n_{\text{Cat}}$ ), where each category  $n$  is described by four prognostic mixing ratio variables:  $Q_{i,\text{tot}}(n)$  (total ice mass),  $Q_{i,\text{rim}}(n)$  (rime ice mass),  $N_{i,\text{tot}}(n)$  (total ice number), and  $B_{i,\text{rim}}(n)$  (rime ice volume). Each ice category is represented by a complete three-parameter gamma PSD of the form

$$N(D) = N_0 D^\mu e^{-\lambda D}, \quad (1)$$

where  $N(D)$  is the number of particles with a maximum dimension  $D$ , and  $N_0$ ,  $\lambda$ , and  $\mu$  are the intercept, slope, and shape parameters, respectively. Since only the one-ice-category configuration is examined in this paper, the category subscript  $n$  is omitted in (1) and hereafter. In the original scheme, the following diagnostic relation is used to prescribe the shape parameter for ice:

$$\mu = 0.0019\lambda^{0.8} - 2, \quad (2)$$

following Heymsfield (2003), where  $\lambda$  is in units of  $\text{m}^{-1}$ , and  $\mu$  is constrained (in P3) to  $0 < \mu < 6$ . The effects of  $\mu$  on the PSD shape are illustrated in Fig. 1, which shows two

TABLE 1. List of symbols.

Symbol	Description	Units
$\rho_i$	Bulk ice density	$\text{kg m}^{-3}$
$\rho_{\text{rim}}$	Rime density	$\text{kg m}^{-3}$
$\mu$	Shape parameter (of gamma PSD)	—
$\mu_{i,\text{init}}$	Shape parameter for new ice (from group 2)	—
$\lambda$	Slope parameter (of gamma PSD)	$\text{m}^{-1}$
$B_{i,\text{rim}}(n)$	Rime volume mixing ratio for ice category $n$	$\text{m}^3 \text{kg}^{-1}$
$D$	Maximum particle dimension	m
$D_{h,\text{max}}$	Maximum diagnosed hail diameter	m
$D_i$	Mass-weighted mean ice diameter	m
$D_{i,\text{limit}}$	Maximum allowable mean-mass ice diameter	m
$D_m$	Mean-mass diameter	m
$F_{\text{rim}}(n)$	Rime mass fraction for ice category $n$	—
$G$	Moment ratio [see (7)]	—
$M_x$	$x$ th moment mixing ratio for ice particles with the same mass as spheres with density $\rho_i$	$\text{m}^x \text{kg}^{-1}$
$n$	Ice category index	—
nCat	Number of ice categories	—
$B_{i,\text{rim}}(n)$	Rime volume mixing ratio for ice category $n$	$\text{m}^3 \text{kg}^{-1}$
$N_{i,\text{tot}}(n)$	Total number mixing ratio for ice category $n$	$\text{kg}^{-1}$
$N(D)$	Number density function (PSD)	$\text{m}^{-1} \text{kg}^{-1}$
$N_0$	Intercept parameter (of gamma PSD)	$\text{m}^{-(1+\mu)} \text{kg}^{-1}$
$Q_c$	Mass mixing ratio of cloud	$\text{kg kg}^{-1}$
$Q_r$	Mass mixing ratio of rain	$\text{kg kg}^{-1}$
$Q_{i,\text{rim}}(n)$	Rime mass mixing ratio for ice category $n$	$\text{kg kg}^{-1}$
$Q_{i,\text{tot}}(n)$	Total mass mixing ratio for ice category $n$	$\text{kg kg}^{-1}$
$Q_{i,\text{tot}}^*(n)$	Normalized mass mixing ratio	kg
$V_{Z,i}(n)$	$M_6$ -weighted fall speed for ice category $n$	$\text{m s}^{-1}$
$w_{\text{max}}$	Peak updraft speed	$\text{m s}^{-1}$
$Z_{\text{advect}}$	Advected variable for prognostic triple-moment [see (12)]	$\text{m}^3 \text{kg}^{-1}$
$Z_e$	Equivalent reflectivity (from model)	dBZ
$Z_{\text{DR}}$	Differential reflectivity (from dual-polarization radar)	dB
$Z_H$	Horizontal reflectivity (from radar)	dBZ
$Z_{i,\text{tot}}(n)$	Reflectivity factor ( $M_6$ ) mixing ratio for spherical ice with equivalent bulk densities for ice category $n$	$\text{m}^6 \text{kg}^{-1}$

hypothetical size distributions with the same mean diameters but different values of  $\mu$ .

Most traditional multimoment BMSs assume constant mass-diameter ( $m$ - $D$ ) parameters for all particle sizes and therefore the remaining PSD parameters can be solved analytically. In contrast, P3 predicts between two and four varying size regimes of the ice PSD, each with different  $m$ - $D$  parameters (see MM15 for details). Because  $\mu$  is derived from  $\lambda$  by (2), which in turn depends on the  $m$ - $D$  parameters, the problem cannot be solved analytically. Instead, a simple root-finding method is employed that finds the combination of PSD values ( $N_0, \mu, \lambda$ ) that minimizes the difference between  $Q_{i,\text{tot}}$  and  $N_{i,\text{tot}}$  computed from integrating the mass distribution (for  $Q_{i,\text{tot}}$ ) and number distribution (for  $N_{i,\text{tot}}$ ) with the actual values of  $Q_{i,\text{tot}}$  and  $N_{i,\text{tot}}$ . To control excessive size sorting of ice that occurs in two-moment schemes with inverse-exponential size distributions (e.g., see MY05a), a stringent upper limit,  $D_{i,\text{limit}}$ , on the mass-weighted mean diameter is imposed by computing the corresponding lower limit of  $\lambda$  and adjusting  $N_{i,\text{tot}}$ , if necessary, to conform to this. Subsequently, all relevant quantities that depend on the ice PSD parameters are computed by numerical integration. These include the microphysical process rates, the moment-weighted bulk fall speeds, and various diagnostic quantities such as the mean bulk density, effective ice radius (used to compute cloud optical properties), and equivalent radar

reflectivity. Note, all quantities in P3 that are determined numerically are precomputed and stored in lookup tables, which are then accessed efficiently during model run time.

Since the original version of the P3 code, this approach has been modified (prior to the three-moment development discussed

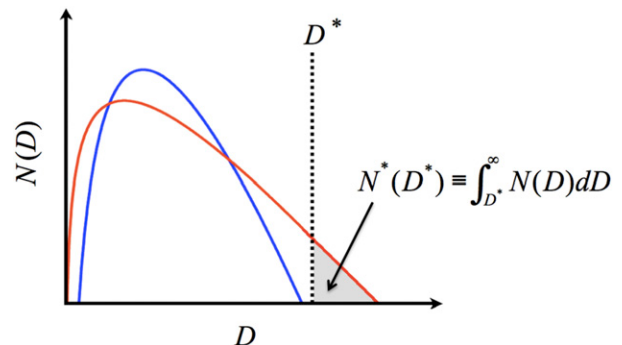


FIG. 1. Illustration of two gamma size distributions, as in Eq. (1). Both have the same mean diameter, but the distribution depicted by the red curve has a lower value of  $\mu$ . The shaded area depicts  $N^*$  (for the red distribution), the total number of particles with  $D > D^*$  (see appendix).

below) such that the lookup table no longer has four dimensions (consistent with the four prognostic ice variables), but rather three: the normalized mass ( $Q_{i\_tot}^* = Q_{i\_tot}/N_{i\_tot}$ ), rime mass fraction ( $F_{rim} = Q_{i\_rim}/Q_{i\_tot}$ ), and rime density ( $\rho_{rim} = Q_{i\_rim}/B_{i\_rim}$ ). This is mathematically equivalent to the original approach that used nonnormalized values of  $Q_{i\_tot}$  and  $N_{i\_tot}$  but reduces the dimensionality of the lookup table by one, improving run-time efficiency. Normalized process rates accessed from the new lookup table are simply multiplied by  $N_{i\_tot}$  during the model time step in the main P3 subroutine.

After updating the prognostic variables based on the microphysical process rates, sedimentation fluxes are computed, based on moment-weighted fall speeds. This is followed by final adjustments and updated values of the prognostic variables at the end of the microphysics time step are thus obtained.

### b. The three-moment ice version

#### 1) THE NEW PROGNOSTIC VARIABLE

A new prognostic equation for a third moment of each ice category has been added to the baseline version of P3. In principle any moment of  $N(D)$ ,  $M_x$ , defined by

$$M_x = \int_0^\infty D^x N(D) dD, \quad (3)$$

can be used as the third prognostic moment in a three-moment scheme in order to treat  $\mu$  as a free parameter. However, the specific combination of prognostic moments is important because the magnitudes of errors in specific nonprognostic moments (resulting from errors in the prognostic moments and hence the PSD parameters), on which microphysical process rates depend, are sensitive to the choice of prognostic moments (e.g., Milbrandt and McTaggart-Cowan 2010). Also, it was shown by Morrison et al. (2016) that only certain combinations of prognostic moments work to preserve important quantities that are functions of these moments. This restricts the choice for a third prognostic moment. Most existing three-moment schemes have used  $M_6$ , the reflectivity factor [with the exception of Tsai and Chen (2020), who use  $M_2$ ], in addition to  $M_0$  (total number) and  $M_3$  (proportional to total mass).<sup>1</sup> Apart from its close relationship to observed radar reflectivity, the original choice of  $M_6$  by MY05a,b was somewhat arbitrary and some other developers of three-moment schemes appear to have followed this approach. As it happens, the  $M_0$ – $M_3$ – $M_6$  combination is a reasonably good choice in terms of minimizing errors for nonprognostic moments (Milbrandt and McTaggart-Cowan 2010). We have therefore chosen  $M_6$  to be the third prognostic moment for ice in the modified P3.

As described below, evolving  $\mu$  independently based on the prediction of  $M_6$  also requires the values of  $M_0$  and  $M_3$ . A subtle but important point about ice in P3 is that due to the different (and variable)  $m$ - $D$  parameters in different parts of the PSD, the total mass mixing ratio  $Q_{i\_tot}$  is not actually proportional to  $M_3$  (as in MY05a,b, for example). In fact,  $Q_{i\_tot}$

is not proportional to any specific moment but rather it is the sum of up to four different partial (incomplete) moments, corresponding to the four possible size regimes in the PSD (see MM15). To overcome the obstacle that  $M_3$  is not a prognostic quantity,  $M_3$  is estimated by using the total mass in the distribution,  $Q_{i\_tot}$ , and the mean bulk density (which is computed numerically and stored in the lookup table), given by

$$\rho_i = \frac{\text{mass}}{\text{volume}} = \frac{\int_0^\infty m(D)N(D) dD}{\int_0^\infty \frac{\pi}{6} D^3 N(D) dD} = \frac{Q_{i\_tot}}{\frac{\pi}{6} M_3}. \quad (4)$$

Rearranging terms, this gives

$$M_3 = \frac{6}{\pi \rho_i} \cdot Q_{i\_tot}. \quad (5)$$

The corresponding moment zero is simply

$$M_0 = N_{i\_tot}. \quad (6)$$

The following equation can be derived from (1) and (3):

$$G(\mu) = \frac{(6 + \mu)(5 + \mu)(4 + \mu)}{(3 + \mu)(2 + \mu)(1 + \mu)} = \frac{M_0 M_6}{(M_3)^2}, \quad (7)$$

where  $M_6$  is the new prognostic moment variable in the three-moment ice formulation for P3.

Since  $M_6$  resembles the radar reflectivity factor (but for a size distribution of constant-density ice spheres, rather than liquid-equivalent particles), we refer to this as  $Z_{i\_tot}$  for notational consistency with  $Q_{i\_tot}$  and  $N_{i\_tot}$ . We emphasize, however, that  $Z_{i\_tot}$  ( $M_6$ ) is *not* the reflectivity factor for ice in P3, which does not assume constant-density spheres, and it is not used to compute the model equivalent radar reflectivity,  $Z_e$  (except indirectly through its effects on the PSD parameters). The value of  $Z_e$  is still computed numerically from the square of the mass of the partial moments of the size distribution (see MM15). Equations (5)–(7) form a system of equations from which  $\mu$  can be solved (numerically), thereby replacing the need for the diagnostic equation, (2). This makes  $\mu$  a fully independent, free parameter. From this value of  $\mu$  and the other four prognostic variables ( $Q_{i\_tot}$ ,  $Q_{i\_rim}$ ,  $N_{i\_tot}$ ,  $B_{i\_rim}$ ), the remaining PSD parameters are then computed. All quantities that depend on the PSD (existing process rates, etc.) are computed numerically as before. This approach requires an additional dimension of the lookup table for obtaining the process rates during model run time; this extra dimension for the three-moment scheme is  $G$  as defined in (7), where  $M_3$  is diagnosed from (5). Note that in (7)  $G$  varies monotonically with  $\mu$  for  $\mu \geq 0$  (where 0 is the lower limit of  $\mu$  in P3), thus the value of  $\mu$  can be computed using a piecewise polynomial approximation, which provides a simple, efficient, and accurate approximation of the analytic cubic root.

### 2) SOURCE/SINK TERMS

For the microphysical tendencies, the prognostic equation for  $Z_{i\_tot}$  (hereafter denoted as  $Z_i$  for convenience in this section, and similarly for  $Q_{i\_tot}$  and  $N_{i\_tot}$ ) is given by

<sup>1</sup> The equivalence of  $M_6$  and the radar reflectivity factor and proportionality of  $M_3$  and total mass is valid for constant-density spherical particles, which is assumed in many bulk schemes.

$$\left. \frac{dZ_i}{dt} \right|_{MP} = \left. \frac{dZ_i}{dt} \right|_{proc\_1} + \left. \frac{dZ_i}{dt} \right|_{proc\_2} + \dots + \left. \frac{dZ_i}{dt} \right|_{sed}, \quad (8)$$

where “proc\_1,” etc., denotes a specific microphysical initiation or growth/decay process and “sedi” denotes sedimentation. Similar to MY05b, each  $Z_i$  tendency term on the right-hand side of (8) belongs to one of three groups:

#### (i) Group 1: Ice initiation processes

For each process by which ice can be initiated, a value  $\mu_{i\_init}$  is specified for the shape parameter of the new portion of ice (from that process only, not the necessarily the final value of  $\mu_i$  if ice is already present). For homogeneous and heterogeneous freezing of cloud or rain,  $\mu_{i\_init}$  is equal to current the value of  $\mu_c$  or  $\mu_r$ , respectively. With this, all three moments are conserved for the conversion of drops to ice, even though the reflectivity moments for cloud and rain are currently diagnostic. If in the future cloud or rain is changed to triple-moment (see Paukert et al. 2019), the  $Z_i$ -tendency formulation will remain the same for drop/droplet freezing.

For heterogeneous (deposition/sorption) nucleation and ice multiplication, an initial value of  $\mu_{i\_init} = 10$  is assumed. This relatively large value of the prescribed value is based on the physical assumption that PSD of the portion of newly nucleated ice will be narrow, given that broad size spectra, with a wide range of particle sizes, are formed from other processes, such as particle breakup and mixing. Since observational guidance on the size distribution of just-nucleated pristine crystals in the atmosphere is limited and likely depends on details of the ice nuclei population which vary widely in time and space, nor is there any theoretical guidance about how to formulate a triple-moment closure for ice nucleation, some closure assumption must be made for  $Z_i$  of the new ice. Note, this is analogous to the necessary closure assumption for  $N_i$  for these processes (in all multimoment schemes), where a small (and arbitrary) mass or size of pristine ice is assumed. Other values of  $\mu_{i\_init}$  have been tested (in the contexts described below) and even with extreme values (0 or 20) the simulation results have virtually no sensitivity. For cases with pure ice clouds, with all crystals originating from heterogenous nucleation and with no riming (e.g., cirrus), the assumed value of  $\mu_{i\_init}$  may have a larger impact.

The  $Z_i$ -tendency equations for processes in group 1 are of the form

$$\left. \frac{dZ_i}{dt} \right|_{proc\_x} = G(\mu_{i\_init}) \left( \left. \frac{dQ_i}{dt} \right|_{proc\_x} \right)^2 \left( \left. \frac{dN_i}{dt} \right|_{proc\_x} \right)^{-1}. \quad (9)$$

#### (ii) Group 2: Growth and decay processes

For all microphysical processes by which an existing population of ice grows or decays, it is assumed that the net change in  $\mu_i$  from these processes is negligible compared to the impact of sedimentation. The  $Z_i$  tendency for such processes is thus obtained from the derivative with respect to time of (7) with  $\mu_i$  is held constant, giving

$$\left. \frac{dZ_i}{dt} \right|_{proc\_x} = G(\mu_i) \left[ 2 \frac{Q_i}{N_i} \left. \frac{dQ_i}{dt} \right|_{proc\_x} - \left( \frac{Q_i}{N_i} \right)^2 \left. \frac{dN_i}{dt} \right|_{proc\_x} \right]. \quad (10)$$

These processes include deposition/sublimation, accretion of cloud or rain, melting, and ice aggregation. The physical interpretation is that the relative spectral dispersion does not change for processes in this group. Strictly speaking, this is an oversimplification since it is known that the spectral dispersion does change for these processes in nature. For example, pure diffusional growth narrows the size spectrum (e.g., Rogers and Yau 1989). For now, we justify this simplification on the grounds that sedimentation is expected to dominate changes to  $\mu_i$ .

The impacts of this simplifying assumption were tested in the context of the 3D supercell simulation discussed below (section 4), whereby all group 2  $(dZ_i/dt)|_{proc\_x}$  processes rates were computed such that  $\mu_i$  tends toward 0 (spectral broadening) or 10 (spectral narrowing) based on the relative change in  $Q_i$  from these processes over some short time scale (here assumed to be equal to the model time step). In both extreme-case tests (broadening and narrowing), the effects on the overall results are very small, thus the closure assumption to derive (10) appears to be reasonable. For weather cases dominated by diffusional growth of ice and where sedimentation (and other processes) are less important, this closure may be less valid. Future work may include relaxing the constant- $\mu_i$  assumption for some group 2 processes and deriving and implementing more detailed  $Z_i$  process rates, as has been done by others (e.g., Yang and Yau 2008; Tsai and Chen 2020). At present, we consider this to be a second-order problem and beyond the scope of this study.

Note that while the group 2 rates do not contribute directly to predicting changes in the shape parameter, all of these process rates do in fact benefit from the fact that  $\mu_i$  varies prognostically since these rates, in particular the mass tendencies, depend on  $\mu_i$  (see MM15). This is analogous to two-moment schemes where some important process rates (e.g., melting, sublimation, and evaporation) have the simplifying assumption of a constant slope ( $\lambda$ ) in the PSD for those particular processes yet the calculation of the rates, in particular the mass tendencies (and thus the corresponding thermodynamic responses), is improved due the fact that the slope varies due to other microphysical processes (e.g., Ziegler 1985; Murakami 1990; Ferrier 1994; Meyers et al. 1997; Reisner et al. 1998; MY05b; Seifert and Beheng 2006; Morrison et al. 2009).

#### (iii) Group 3: Sedimentation

The  $Z_i$  tendency due to sedimentation is computed using the standard 1D flux of  $Z_i$ , which is given by

$$\left. \frac{dZ_i}{dt} \right|_{sed} = \frac{1}{\rho} \frac{\partial (\rho Z_i V_{z,i})}{\partial z}, \quad (11)$$

where  $V_{z,i}$  is the sixth-moment-weighted bulk fall speed (e.g., see MY05b). As with the mass-weighted and number-weighted fall speeds, the calculation of  $V_{z,i}$  involves the numerical integration over all sizes since the integral equation includes the terminal fall speed for a single particle  $V(D)$ , which is a complicated function of  $D$  and depends on the size-regime-dependent and projected area-diameter relations (see section 2a and MM15).

### 3) CATEGORY MERGING

In the multi-ice-category P3 configuration (i.e., for  $n_{\text{Cat}} > 1$ ), there exists the possibility for the ice in two separate categories to merge into a single category if, at the end of the time step, the overall physical properties of the two populations of ice are deemed to be sufficiently similar (see Milbrandt and Morrison 2016). In such cases, the values of each prognostic variable for the two categories are simply summed and assigned as the values of the new merged category. With the three-moment ice configuration, this now includes  $Z_i$ . Physically, this has the effect of resulting in a broader combined size distribution (and a smaller value of  $\mu_i$ ) than either of the two initial distributions (e.g., see Milbrandt and Yau 2006a, their Fig. 20). Note, the treatment of  $Z_i$  for ice category merging is included here to provide a complete description of the three-moment ice in P3; however, the remainder of this study is restricted to the single-category configuration. The impacts of the combined effects of three-moment and multcategory ice in P3 will be examined a future study.

### 4) RELAXED MEAN SIZE LIMITER

In the original P3 scheme, size sorting of ice was controlled by imposing a strict upper limit to the mean ice size  $D_m$ , with a value of  $D_{i,\text{limit}} = 2 \text{ mm}$ . In the three-moment version this strict limit is no longer necessary (and is undesirable), thus  $D_{i,\text{limit}}$  has been set to a very large value (400 mm). It is expected, however, that in practice  $D_m$  will never reach this limit, so for all practical purposes no upper limit is imposed.

### 5) TREATMENT BY DYNAMICS

The advection and diffusion of  $Z_{i,\text{tot}}$  in the modified P3 is treated slightly differently compared to MY05a,b and other three-moment schemes. While quantities are still advected and diffused by the model dynamics in the standard way (i.e., as with all other non-mass-loading hydrometeor scalars), rather than passing  $Z_{i,\text{tot}}$  back to the dynamics as the prognostic variable to be transported by the dynamics, advection/diffusion is performed on the quantity  $Z_{\text{adve}}^*$ , given by

$$Z_{\text{adve}}^* = (N_{i,\text{tot}} \cdot Z_{i,\text{tot}})^{0.5}. \quad (12)$$

This quantity is computed at the end of the microphysics time step and passed to the dynamics, which transports  $Z_{\text{adve}}^*$ . At the next microphysics time step, P3 receives the updated  $Z_{\text{adve}}^*$  and computes  $Z_{i,\text{tot}}$  from (12). It was shown theoretically in Morrison et al. (2016) and with numerical simulations in Paukert et al. (2019) that for three-moment schemes this approach works better to preserve important diagnostic quantities during advection, including all the PSD parameters, which are derived from the prognostic variables. The effects of this are illustrated in section 5.

## 3. Idealized 1D simulations

### a. Experimental design

To illustrate the effects of the three-moment ice configuration of P3 in a simple context, idealized “hailstorm”

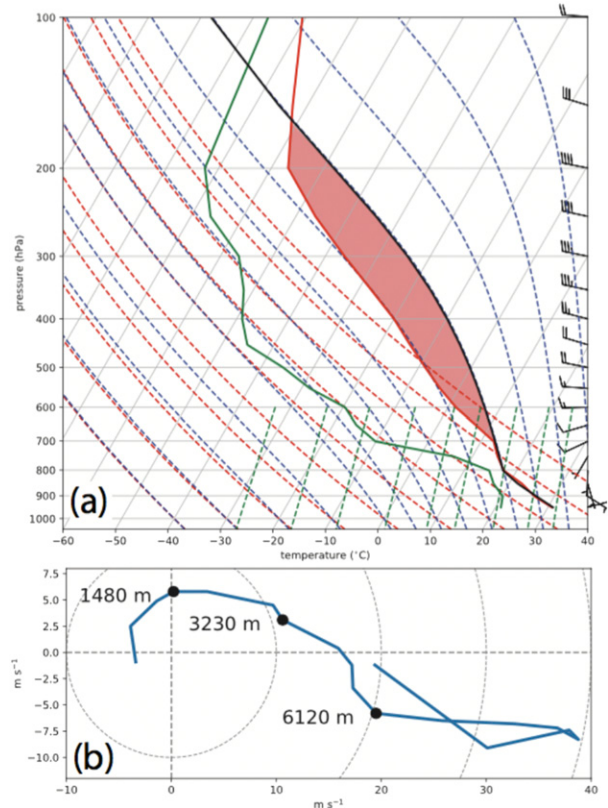


FIG. 2. Initial (a) skew  $T$  and (b) hodograph, taken from the RUC point sounding valid at 0100 UTC 1 Jun 2008. The surface-based CAPE (depicted in red shading) is  $3937 \text{ J kg}^{-1}$ .

simulations were conducted using a 1D kinematic cloud model, described in Milbrandt et al. (2014). The temperature and water vapor mixing ratio are initialized from a sounding (Fig. 2). A time- and height-varying updraft profile is prescribed, with a peak value of  $5 \text{ m s}^{-1}$ . At each time step, the model computes advection, compression, and divergence of temperature, water vapor, and all (subsequently formed) hydrometeor fields; it computes adiabatic cooling; finally, it calls the microphysics scheme. In these simulations hail is produced (see below) even though the peak updraft speed is far too low to support hail production in nature or in a detailed dynamical model. However, note that this is a highly idealized model configuration (e.g., with no entrainment, shear, mixing) and the purpose is just to illustrate the effects of changes to the microphysics scheme in a simple, controlled context before proceeding to examine this in a more realistic testing ground (section 4).

Simulations were run with the two-moment ice configuration of P3 with the original mean size limiter (hereafter 2-MOM\_DLIM), the two-moment configuration with the relaxed size limiter (2-MOM), and the new three-moment ice version, also with the relaxed size limiter (3-MOM); see Table 2. Prognostic and diagnostic fields were output every time step in order to produce time-height plots, discussed below.

TABLE 2. List of P3 configurations (simulations).

Configuration name	Description
2-MOM_DLIM	Two-moment ice; original $D_{i,\text{limit}}$ (2 mm)
2-MOM	Two-moment ice; relaxed $D_{i,\text{limit}}$ (400 mm)
3-MOM	Three-moment ice; relaxed $D_{i,\text{limit}}$
2-MOM_DIAGMU	Two-moment ice; relaxed $D_{i,\text{limit}}$ ; new diagnostic- $\mu_i$
3-MOM_ADVZ	Three-moment ice; relaxed $D_{i,\text{limit}}$ ; advection/diffusion of $Z_{i,\text{tot}}$

### b. Simulation results

Results from the three 1D simulations are shown in Fig. 3, which summarizes the evolution of the prescribed vertical motion and surface liquid and solid precipitation rates (row 1), cloud and rain mixing ratios ( $Q_c$  and  $Q_r$ , row 2), total ice mass ( $Q_{i,\text{tot}}$ , row 3), ice shape parameter ( $\mu_i$ , row 4), the mass-weighted mean ice diameter ( $D_m$ , row 5), the estimated maximum hail diameter ( $D_{h,\text{max}}$ , row 6), and the equivalent reflectivity ( $Z_e$ , row 7). The details for the calculations of the diagnostic  $D_{h,\text{max}}$  are described in the appendix. In all runs, ascent produces adiabatic cooling, condensation to cloud water (Figs. 3d–f), ice initiation after 20 min (Figs. 3g–i), accretional growth of ice, sedimentation of ice through the updraft (which later decreases in strength), and partial melting to rain (Figs. 3d–f). Note, in these idealized simulations, the ice that falls through the updraft and reaches the melting level (or the surface) is high density and fully rimed and can thus be interpreted as hail.

In 2-MOM\_DLIM,  $\mu_i$  is 0 everywhere except at upper levels (Fig. 3j),  $D_m$  never gets larger than 10 mm (Fig. 3m),  $D_{h,\text{max}}$  has a peak value around 35 mm (Fig. 3p), and peak  $Z_e$  values are less than 60 dBZ (Fig. 3s). In 2-MOM with the relaxed  $D_{i,\text{max}}$ ,  $\mu_i$  is nearly identical to 2-MOM\_DLIM; however, there are much larger values of  $D_m$  (40–45 mm; Fig. 3n),  $D_{h,\text{max}}$  (80–90 mm; Fig. 3q), and  $Z_e$  (65–70 dBZ; Fig. 3t). This is consistent with previous studies with realistic 3D simulations which show that when hail is constrained to have an inverse-exponential PSD ( $\mu_i = 0$ ), but allowed to have large mean diameters, excessive gravitational size sorting leads to large mean and maximum hail sizes and extremely high reflectivities (e.g., Milbrandt and Yau 2006b; Dawson et al. 2014). In the original two-moment-ice P3 (2-MOM\_DLIM), this problem is controlled through the stringent  $D_{h,\text{max}}$ , which prevents the PSD from becoming too broad; however, this does not allow for the simulation of large ice/hail, as illustrated in Johnson et al. (2019).

In 3-MOM, size sorting results in a more realistic narrowing of the PSD (i.e., increasing  $\mu_i$  values; Fig. 3l), as expected, which thereafter prevents excessive size sorting by reducing the ratio of the mass-weighted to number-weighted bulk fall speeds (see Milbrandt and McTaggart-Cowan 2010). This results in smaller values of  $D_m$  (20–25 mm; Fig. 3o),  $D_{h,\text{max}}$  (50–60 mm; Fig. 3r), and  $Z_e$  (60–65 dBZ; Fig. 3u) compared to 2-MOM, but all of which are larger than 2-MOM\_DLIM.

Based on the tests in the simple 1D model context, the new three-moment ice version of P3 appears to work correctly and

accomplishes the primary objectives of this modification. Gravitational size sorting of ice is now physically controlled by allowing the spectral dispersion to vary freely without a stringent limitation on the mean particle size, thus allowing the production of large ice/hail but without generating unrealistically large sizes and overly high reflectivity values. We may now proceed to examine the behavior of the modified scheme in a more complex and realistic model environment.

## 4. Quasi-idealized 3D supercell simulations

### a. Case description

For the 3D idealized supercell case, simulations were run for the 1 June 2008 central Oklahoma supercell case. This storm formed in an environment characterized by deep (0–6 km) west-northwesterly shear  $> 20 \text{ m s}^{-1}$  and abundant low-level moisture leading to a high amount of surface-based CAPE (see below). The storm moved southeasterly during the late evening of 30 May and was observed by the KOUN polarimetric radar in Normal, Oklahoma. Kumjian et al. (2010) provide a detailed description of the microphysical evolution of the storm as revealed by polarimetric observations, noting that the storm maintained a well-defined and persistent low- $Z_{\text{DR}}$  hail signature for much of its life (e.g., Fig. 4), and that hailstones of nearly 10 cm in diameter were observed at the surface. Additional details on the evolution of this storm and its environment are provided in Kumjian et al. (2010) and Dawson et al. (2014).

Dawson et al. (2014) performed idealized simulations of this storm to investigate the relative importance of size sorting of hail and rain with a three-moment scheme. This case is therefore suitable for the purposes of testing the new three-moment-ice version of P3. In the simulations discussed below (as well as the 1D simulations discussed above), the sounding used (Fig. 2) is the same as that used in Dawson et al. (2014) which was extracted from the 0100 UTC 1 June 2008 Rapid Update Cycle (RUC) analysis near the region of the observed initiation of the storm.

### b. Experimental design

Idealized cloud-resolving 3D simulations were run using the same configurations of P3 as for the 1D runs described above, plus others (see Table 2). These simulations were performed using the Weather Research and Forecasting (WRF) compressible, nonhydrostatic atmospheric model, version 3.9.1 (Skamarock et al. 2008). A quasi-idealized model case setup was used, with the RUC model sounding described above (Fig. 2) to provide the horizontally homogeneous initial thermodynamic and wind conditions. Convection was initiated using the vertical velocity forcing method of Naylor and Gilmore (2012) which nudges the vertical velocity to  $10 \text{ m s}^{-1}$  with a nudging time scale equal to the model time step. Nudging was applied for the first 15 min of the simulations to an ellipsoid region with a horizontal radius of 15 km and vertical radius of 1.5 km, centered at 1.5 km AGL, with a cosine decay to zero nudging along the ellipsoid edge.

A horizontal grid spacing of 250 m was used, with a vertical grid spacing of approximately 250 m with a slight grid

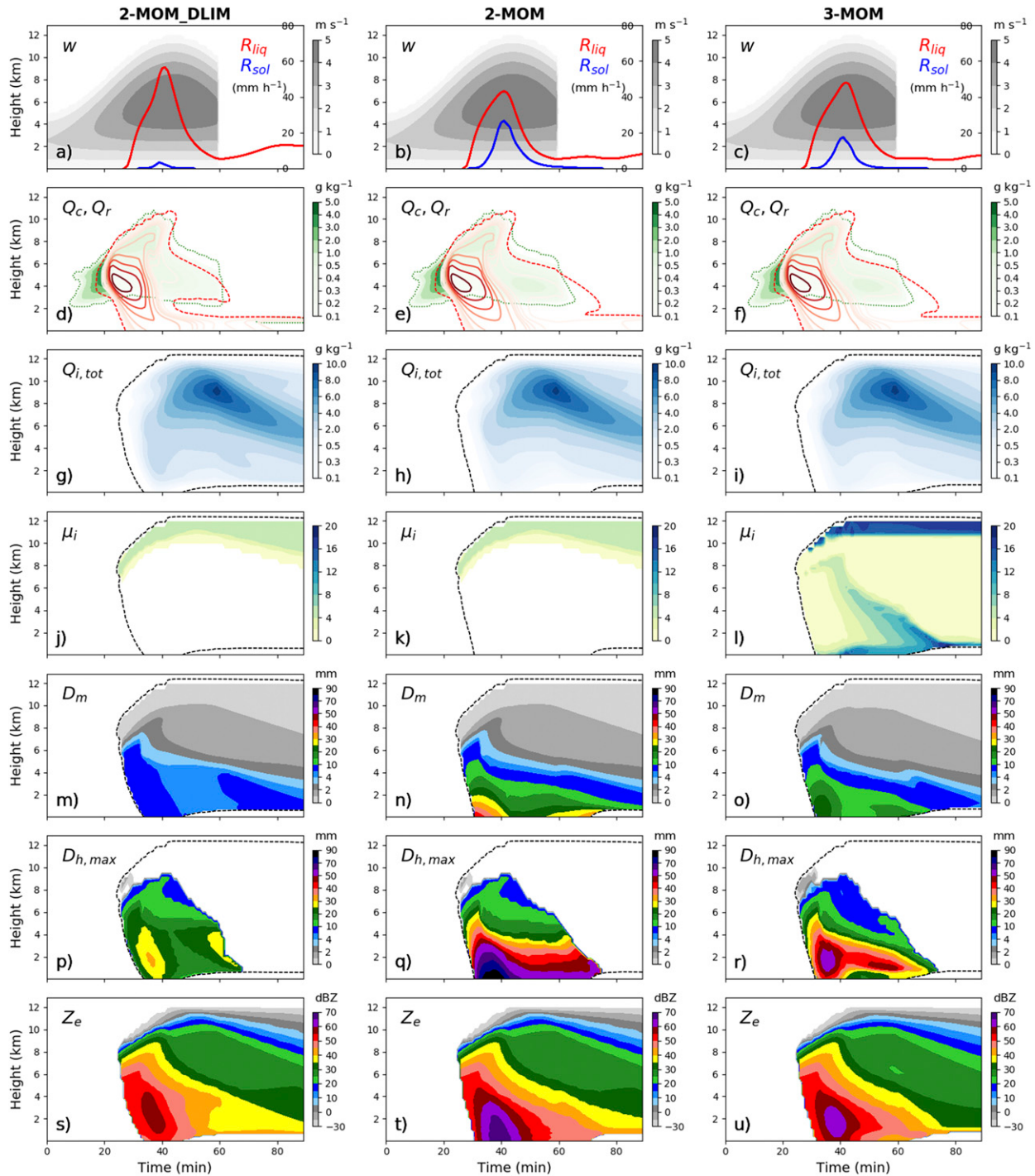


FIG. 3. Time–height plots from the 1D simulations for (left) 2-MOM\_DLIM, (center) 2-MOM, and (right) 3-MOM. The fields shown are vertical motion (shading) and liquid (red) and solid (blue) (a)–(c) precipitation rates ( $w$ ,  $R_{\text{liq}}$ ,  $R_{\text{sol}}$ ), (d)–(f) cloud and rain mixing ratios ( $Q_c$  and  $Q_r$ ), (g)–(i) total ice mixing ratio ( $Q_{i,\text{tot}}$ ), (j)–(l) the ice shape parameter ( $\mu_i$ ), (m)–(o) the mean-mass ice diameter ( $D_m$ ), (p)–(r) the maximum hail diameter ( $D_{h,\text{max}}$ ), and (s)–(u) the equivalent reflectivity ( $Z_e$ ). The red contour intervals for  $Q_r$  in (d)–(f) match the green shading intervals for  $Q_c$ .

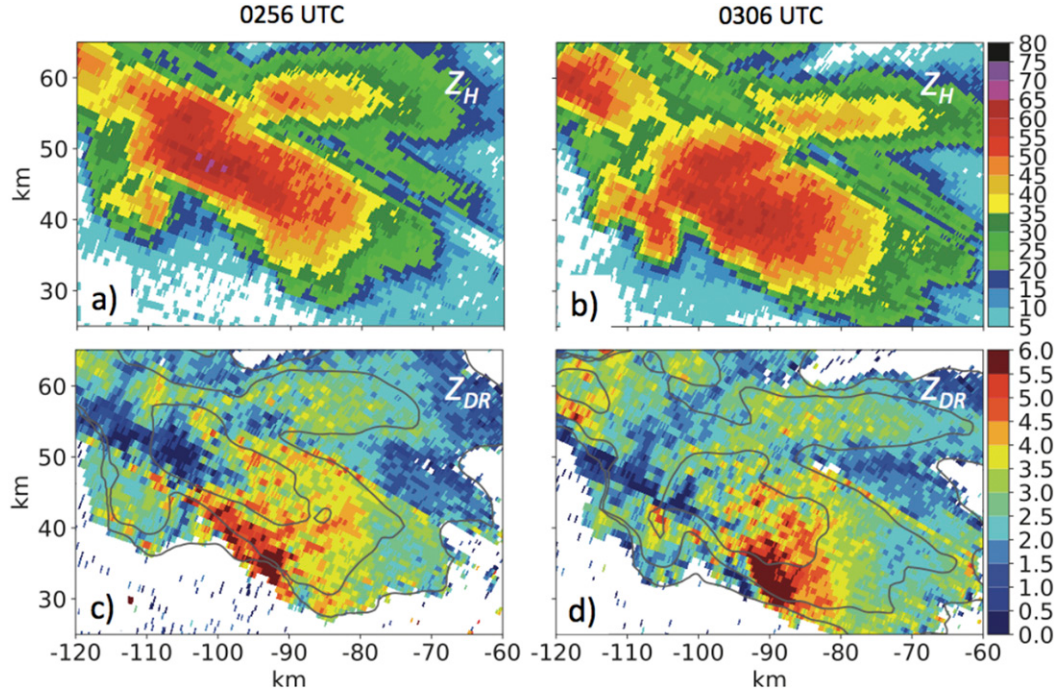


FIG. 4. Observed (a),(b) horizontal reflectivity [ $Z_H$  (in dBZ)] and (c),(d) differential reflectivity [ $Z_{DR}$  (in dB)] at (a),(c) 0256 and (b),(d) 0306 UTC 1 Jun 2008 from the KOUN polarimetric radar ( $0^\circ$  elevation) for the 1 Jun 2008 Oklahoma supercell.

stretching from the surface to model top. Advection of microphysical variables used the fifth- and third-order options for the horizontal and vertical, respectively, with a monotonic limiter (Wang et al. 2009). Subgrid-scale mixing was treated using the predicted turbulent kinetic energy option in WRF. Previous studies have shown that this configuration, or similar configurations in other models, can reasonably resolve deep convective updraft features and begin to represent an inertial subrange of turbulence using 250-m grid spacing (e.g., Bryan et al. 2003; Bryan and Morrison 2012; Lebo and Morrison 2015). The computational domain was  $150 \times 150 \times 24 \text{ km}^3$ . The model time step was 2 s. Open lateral boundary conditions and a free-slip lower boundary were used. The top boundary was a rigid lid with a Rayleigh damper applied to the uppermost 5 km. Surface fluxes and radiation were neglected.

### c. Results

The general evolution of the simulated storm is illustrated in Fig. 5, which shows the column-maximum  $Z_e$  at various integration times between 20 and 55 min for the 3-MOM run. The domain-maximum updraft and downdraft velocities for 2-MOM\_DLIM, 2-MOM, and 3-MOM are shown in Fig. 6. After the initial shock from the forced convection and a spin-up period lasting approximately 35 min (based on the symmetrical shape of the reflectivity and the increasing peak updraft speed), the modeled storms have relatively steady peak updrafts around  $50 \text{ m s}^{-1}$ , splitting into two main storms. After 55 min (not shown), the storm begins to decay. The updraft strength during the quasi-steady period is comparable

to what one would estimate from the initial sounding (Fig. 2), with a surface-based CAPE of  $3937 \text{ kg m}^{-2}$ , giving an estimated peak vertical velocity  $w_{\max}$  of  $44 \text{ m s}^{-1}$  based on the standard rule-of-thumb estimate of  $w_{\max} \sim 0.5\sqrt{(2 \times \text{CAPE})}$ .

The vertical structure of the model reflectivity for 3-MOM (as well as the two-moment runs, discussed below) at 35 and 55 min are shown in Figs. 7 and 8, respectively (right columns). The overall storm structure is reasonable and compares fairly well to the observed storm (Kumjian et al. 2010; Dawson et al. 2014). However, the  $Z_e$  values at lower levels in the downshear forward flank region, under the anvil (e.g., Fig. 8c; at  $\sim 60 < x < 100 \text{ km}$  and  $z < 3 \text{ km}$ ), appear to be unrealistically high, given that supercells typically do not have precipitation reaching the ground in those regions (e.g., Lemon and Doswell 1979). This appears to originate from the WRF Model setup, which results in excessive transport of condensate into that region. That is, the downshear reflectivity is not indicative of any deficiencies in the microphysics scheme. This was verified by rerunning the simulation with three other multimoment BMSs in WRF (Thompson, Morrison, and NSSL); all runs exhibit a similar pattern of excessive reflectivity under the anvil, to varying degrees (not shown). Thus, while this is somewhat unsatisfactory in terms of producing a completely realistic supercell in all aspects, the simulations are sufficiently realistic for the purpose of this study, to illustrate the effects of triple-moment ice in the P3 scheme. We note in passing that the high downshear reflectivity values are all under the melting layer and thus another possible contributing factor may be the representation of rain. This may be improved by a better parameterization of ice

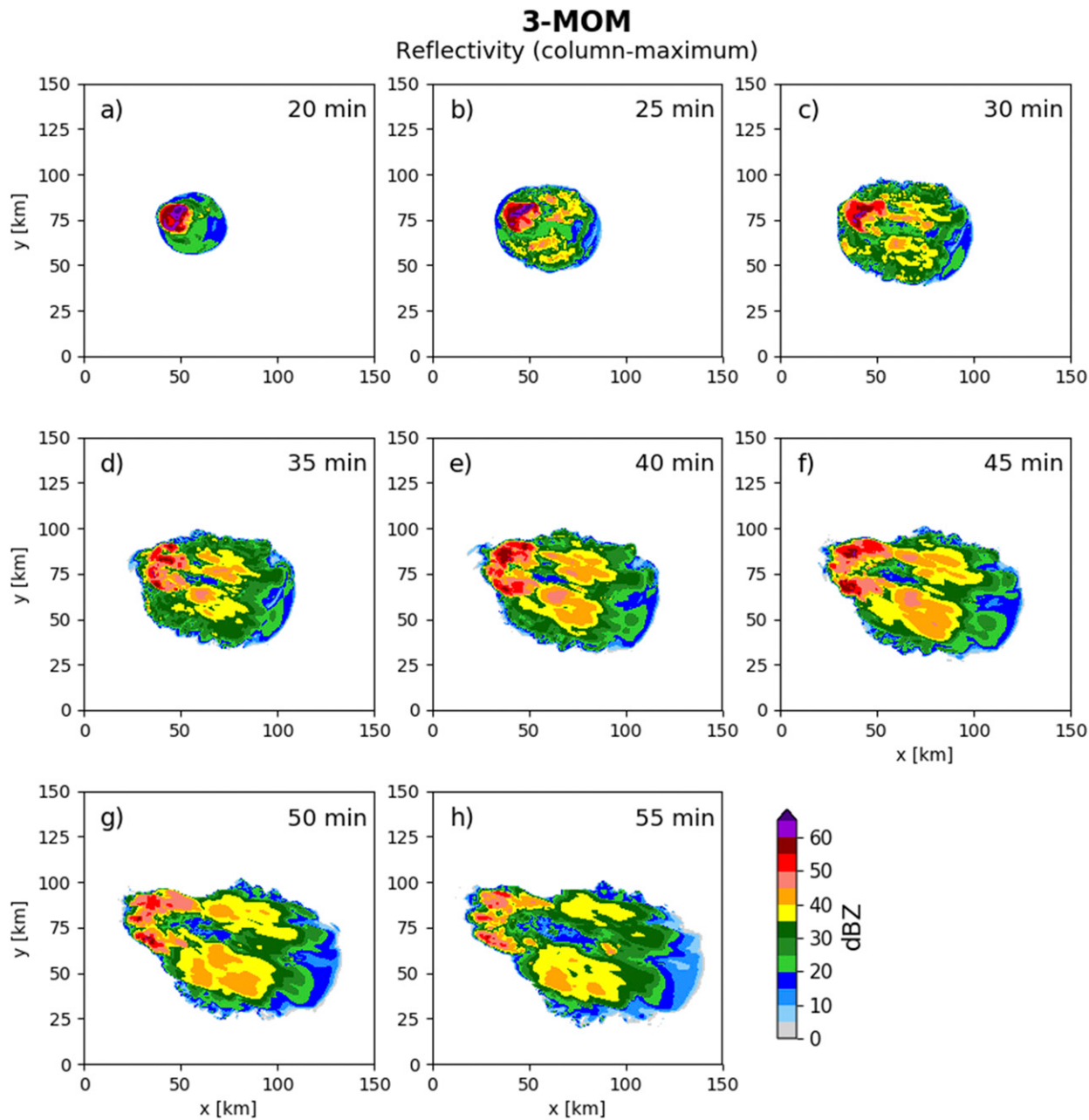


FIG. 5. Equivalent reflectivity ( $Z_e$ , 1 km AGL) from the 250-m WRF simulation using 3-MOM. The integration times are indicated in each panel.

melting in P3 (e.g., Cholette et al. 2019) and a three-moment treatment of rain (e.g., Paukert et al. 2019); this will be examined in future work.

The peak  $Z_e$  values of around 55 dBZ in the convective core (Fig. 8c) and the areal coverage (Fig. 8f) of values  $>35$  dBZ for 3-MOM compare reasonably well to the observed storm (Fig. 4) though the actual peak values as well as the areal coverage of high  $Z_e$  ( $>50$  dBZ) are slightly lower than observed. This underestimation is not a great concern, given that, for example, the version of P3 used in this study lacks a

predicted liquid fraction of mixed-phase particles (as in Cholette et al. 2019) and thus it would be expected to underestimate the reflectivity contribution from wet hail, which has higher reflectivity than dry hail due to the higher dielectric factor of water than ice (Smith 1984). Dilution of particle properties due to the use of a single ice category may also play a role (see discussion below). That said, the reflectivity structure in the convective core regions from the three-moment ice P3 simulation is realistic, including having a well-defined bounded weak-echo region [Fig. 8c; at approximately

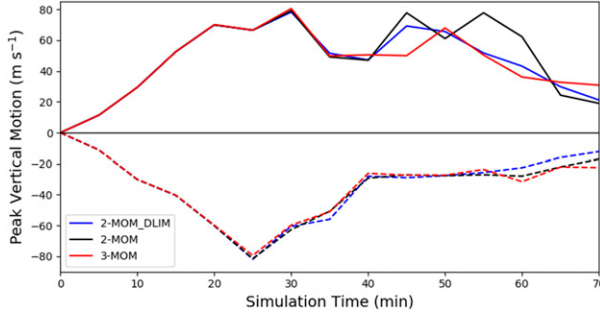


FIG. 6. Domain-maximum updraft (solid) and downdraft (dashed) velocities from 250-m simulations for 2-MOM\_DLIM (blue), 2-MOM (black), and 3-MOM (red).

$(x, z) = (35 \text{ km}, 5 \text{ km})$ ] which is typical of well-organized hailstorms (e.g., Lemon and Doswell 1979). Comparing 3-MOM to the original and modified two-moment runs, the differences in  $Z_e$  are qualitatively similar to the 1D results discussed in section 3;

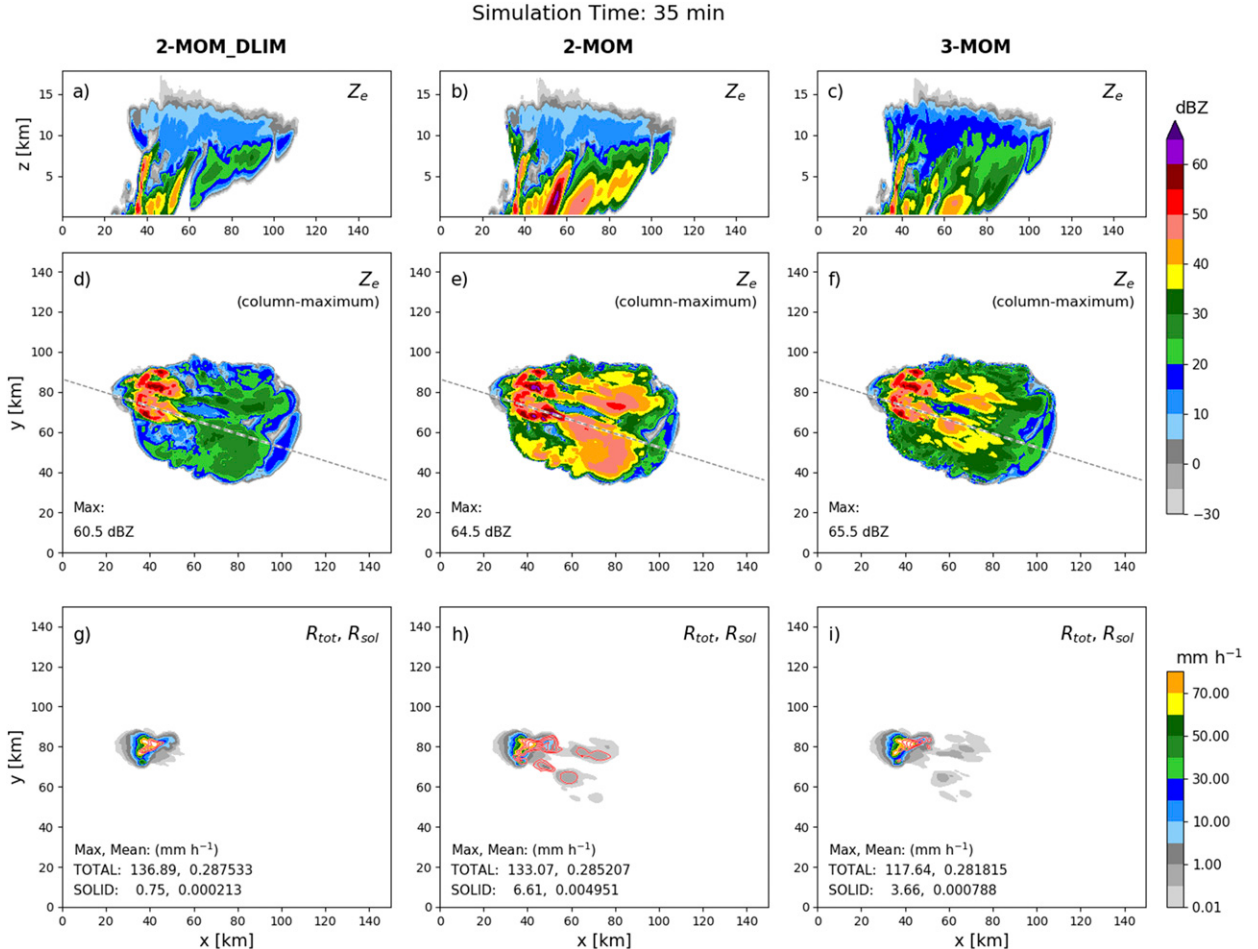


FIG. 7. (a)–(f) Equivalent reflectivity ( $Z_e$ ) at 35 min for the (a),(d) 2-MOM\_DLIM, (b),(e) 2-MOM, and (c),(f) 3-MOM 250-m simulations. (a)–(c) Vertical cross sections along diagonal path indicated in (d)–(f), which show column-maximum reflectivity. (g)–(i) The 5-min-averaged (from 30 to 35 min) total (shading) and solid (red contours) precipitation rates ( $R_{\text{tot}}$  and  $R_{\text{sol}}$ ), centered at 35 min. Contours for  $R_{\text{sol}}$  match the shading intervals for  $R_{\text{tot}}$  ( $0.01, 0.1, 1, 5, 10, 20, \dots \text{ mm h}^{-1}$ ). Domain-maximum and mean values are indicated in the panels.

2-MOM\_DLIM has lower  $Z_e$  values and those from 2-MOM are much higher. Also, the two-moment runs have slightly lower  $Z_e$  values than 3-MOM at upper levels, which is likely a result of the high values of  $\mu_i$  there (see below) that result from the use of (2).

The bottom panels of Figs. 7 and 8 show the total and solid 5-min averaged precipitation rates ( $R_{\text{tot}}$  and  $R_{\text{sol}}$ , respectively), ending at the specified simulation times, along with domain-maximum and domain-mean values indicated in the corners. At the mature stage (55 min) the total precipitation patterns and values are similar for all simulation, though with broader coverage of precipitation (but with small values) in the downshear regions of 2-MOM and 3-MOM (Figs. 8h,i;  $x > 50 \text{ km}$ ). On the other hand, the solid (hail) precipitation is notably different. The mean and maximum  $R_{\text{sol}}$  values for 3-MOM are around double those of 2-MOM\_DLIM, while the values and coverage are notably higher in 2-MOM, with solid precipitation even reaching the surface in the anvil region [Fig. 8h;  $(x, y) \sim (60 \text{ km}, 50 \text{ km})$ ]. This is consistent with the impacts on the simulated ice PSDs in the various configurations

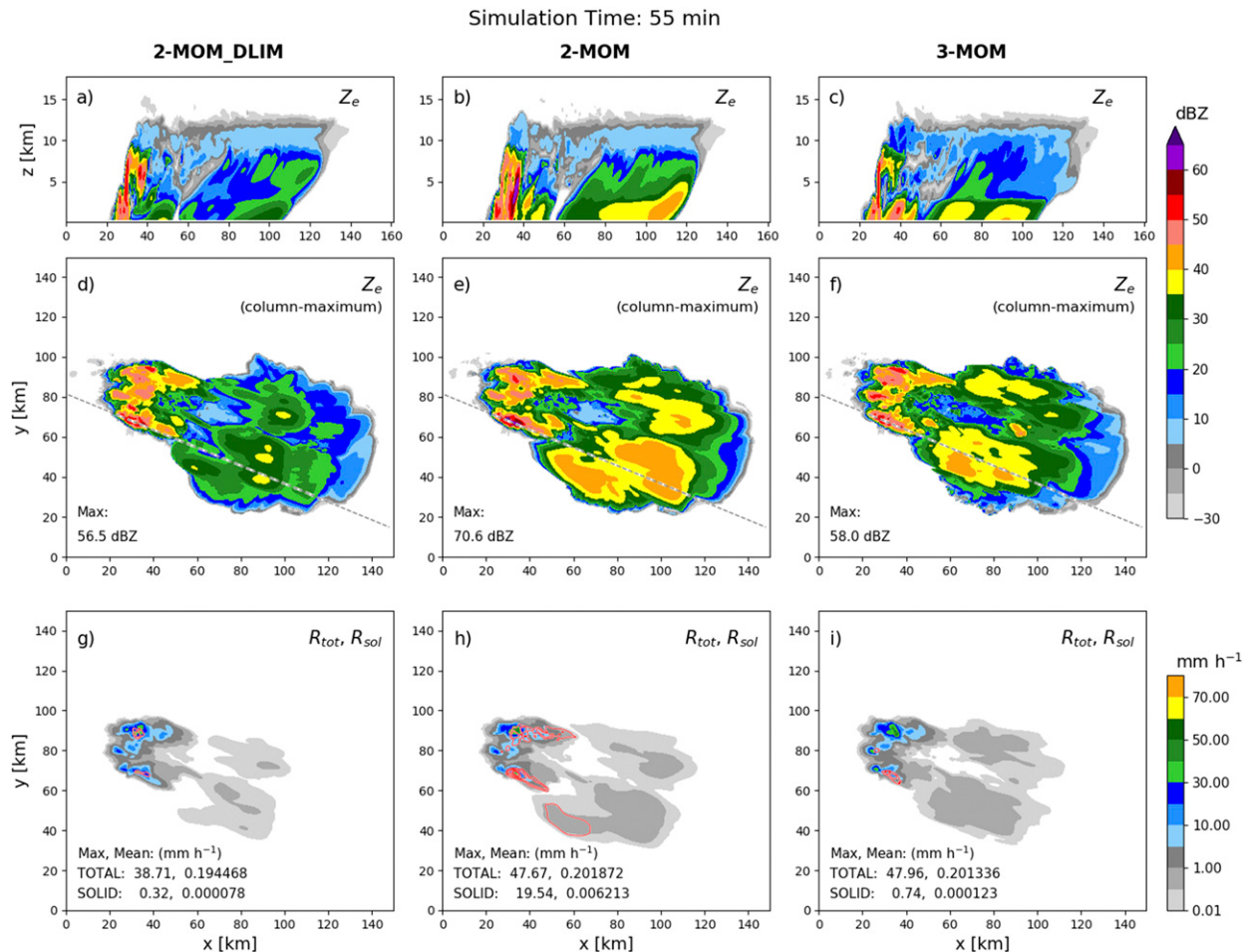


FIG. 8. As in Fig. 7, but for simulation time 55 min.

and the extent to which the production of large mean sizes is possible yet physically controlled.

Figure 9 shows vertical cross sections of various parameters related to the ice fields from the three simulations at the mature phase (55 min). Again, the overall differences are qualitatively similar to the 1D results. The spatial distribution of ice mass is broadly similar in all simulations, though with somewhat lower values in the anvil for 3-MOM (Figs. 9a–c). In both two-moment simulations,  $\mu_i$  values greater than 1 appear only at upper-levels, with values of 0 elsewhere (Figs. 9d,e). In contrast,  $\mu_i$  in 3-MOM generally has high values at lower levels owing to size sorting whereas at higher levels mixing, which broadens the PSD and lowers the value of  $\mu_i$  (see Milbrandt and Yau 2006a), appears to dominate (Fig. 9f). The distribution of bulk particle density (Figs. 9g–i) is similar for all runs, with the highest values concentrated in the convective core region ( $\sim 30$ – $40$  km), though with a broader region of high values for 2-MOM, moderately high values at the highest and lowest elevations in the anvil region and the lowest values at midlevels downshear of the convective core. In 2-MOM, values of  $\mu_i$  of 0 in the convective core below 5 km (Fig. 9e) combined with the unrestricted maximum mean ice size leads to excessive size

sorting, which is evident from the large  $D_m$  values (Fig. 9k), and thus high terminal fall speeds (not shown) and riming growth rates and densification. This accounts for the broader area of high mean density (Fig. 9h) compared to the other runs (Figs. 9g,i), and illustrates the reason for the large  $R_{sol}$  values in 2-MOM (Fig. 8h).

For 2-MOM\_DLIM, the peak  $D_m$  values are less than 10 mm (Fig. 9j) and peak values of  $D_{h,max}$  are less than 25 mm (Fig. 9m). Although the  $D_{h,max}$  diagnostic is somewhat subjectively defined (see appendix), these values are probably too low for such an intense storm. Furthermore, no hail at all reaches the surface for this run (Fig. 9a). With the relaxation of  $D_{i,limit}$ , excessive size sorting results in much larger mean sizes in 2-MOM (up to 50 mm; Fig. 9k) and maximum hail sizes (Fig. 9n) and with hail reaching the surface over a broad region, including under the anvil. With 3-MOM, the narrowing of the PSD (i.e., increased  $\mu_i$  values) from size sorting—which is kept under control as a result—prevents both  $D_m$  (Fig. 9l) and  $D_{h,max}$  (Fig. 9o) from becoming excessively large, though allowing for considerably larger sizes than in the overly restrictive original two-moment configuration (2-MOM\_DLIM). Also, the spatial distribution of hail reaching the surface (i.e., the width of

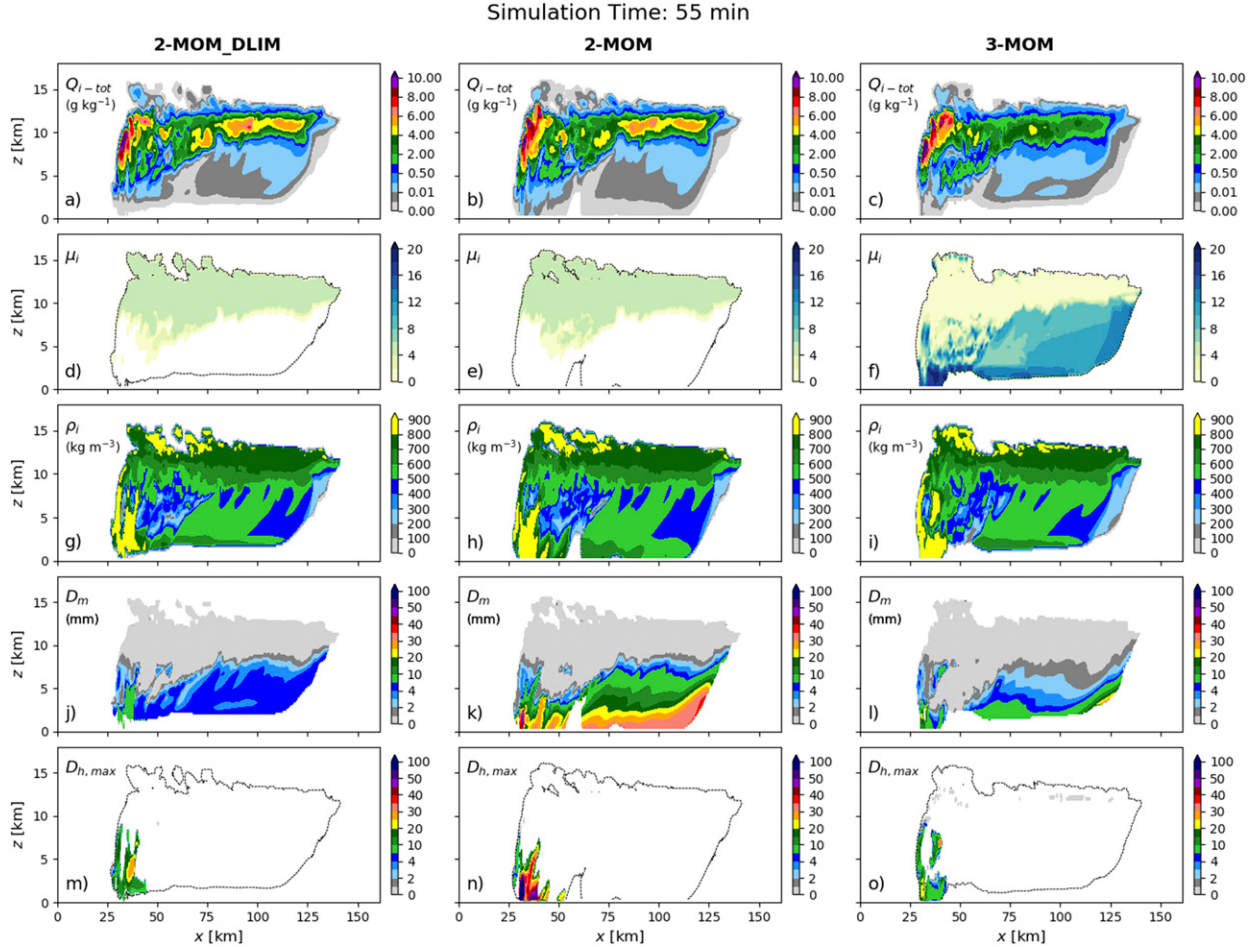


FIG. 9. (a)–(c)  $Q_{i,\text{tot}}$ , (d)–(f)  $\mu_i$ , (g)–(i)  $\rho_i$ , (j)–(l)  $D_m$ , and (m)–(o)  $D_{h,\text{max}}$  for the (left) 2-MOM\_DLIM, (center) 2-MOM, and (right) 3-MOM 250-m simulations at 55 min. The dashed lines denote a  $Q_{i,\text{tot}}$  value of  $10^{-3} \text{ g kg}^{-1}$ .

the hail shaft) is arguably the most realistic in 3-MOM, with a core ( $Q_{i,\text{tot}} > 0.01 \text{ g kg}^{-1}$  at the surface) of a few kilometers wide and a broader region of lower values of small hail extending to  $\sim 10 \text{ km}$ , all in the convective core region, and with no hail reaching the surface in the anvil region (Fig. 9o), unlike in 2-MOM (Fig. 9n).

The impact on simulated hail at low elevations in the convective core at 1 km AGL from the three simulations at 55 min is shown in Fig. 10. The presence of large hail in real storms can be identified from dual-polarized radar as regions with  $Z_H > 35 \text{ dBZ}$  and  $Z_{DR} < 0.5 \text{ dB}$  (e.g., Kumjian et al. 2010) and is evident from radar observations of the 1 June 2008 storm (Fig. 4). For comparison to the radar observations, the low-level (approximately 1 km AGL) simulated reflectivity and maximum diagnosed hail size (see appendix) are shown in Fig. 10, where total ice mass is considered to be hail according to the criteria described in the appendix. Note that the simulations presented are idealized and direct comparison/evaluation against observations should be done in a general sense only, and not overly quantitatively. For 2-MOM\_DLIM (Fig. 10, left), the  $Z_e$  values are reasonable (peak value of 52.4 dBZ). For 2-MOM (Fig. 10, middle) the reflectivity values are much larger (peak

value of 66.4 dBZ), especially given that wet hail is not considered in the model calculations, and the region with hail is much larger than what is deduced from radar (Fig. 4). The 3-MOM simulation (Fig. 10, right) appears to have a realistic  $Z_e$  pattern (peak value of 52.4 dBZ) and spatial pattern of hail. The maximum simulated hail sizes at that elevation were 21, 162, and 53 mm for 2-MOM\_DLIM, 2-MOM, and 3-MOM, respectively. Overall, the combination of the relaxed mean ice size limiter with the three-moment treatment of ice appears to lead to a generally improved simulation of hail and related fields in P3.

## 5. Discussion

### a. Alternative diagnostic- $\mu_i$ relation for the two-moment ice configuration

As discussed in section 2, one of the motivations for implementing a three-moment representation of ice in P3 was the need to relax the stringent mean size limiter while still controlling gravitational size sorting through an independently varying  $\mu$ . The original diagnostic- $\mu$  relation, (2), is limited in this regard since it gives increasingly narrow PSDs (larger  $\mu$ ) for decreasing mean sizes but becomes an inverse-exponential

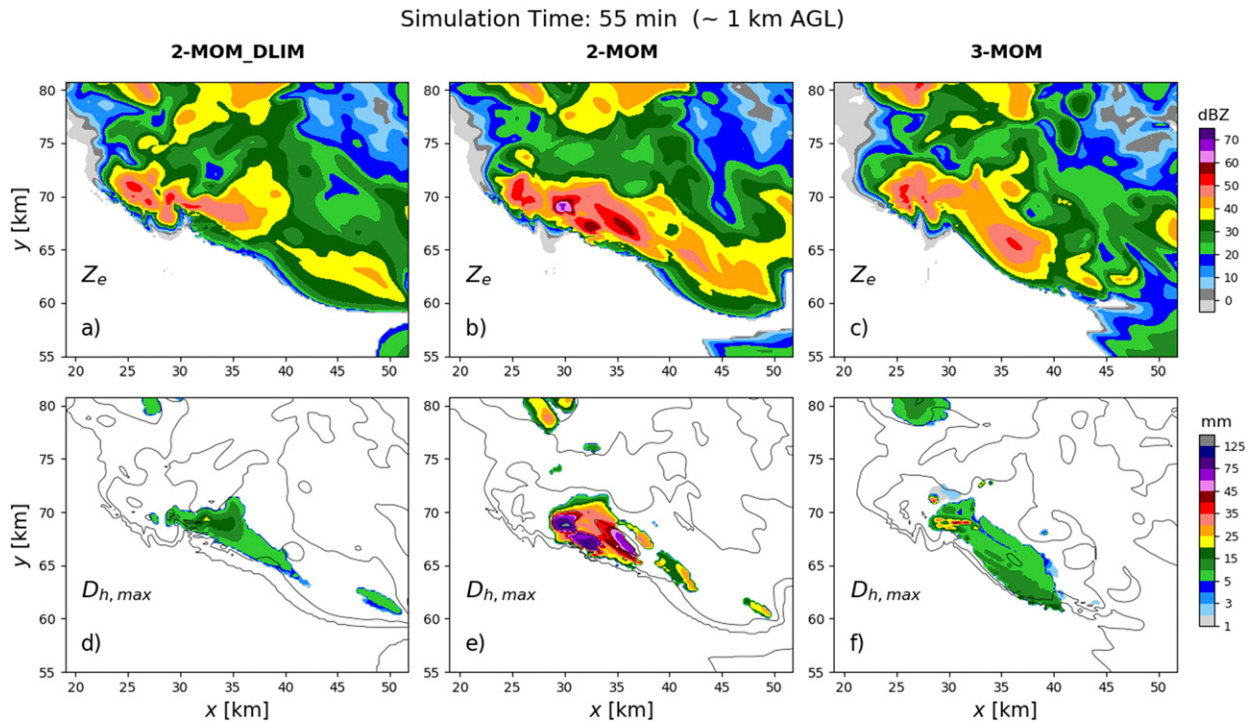


FIG. 10. (a)–(c) Equivalent reflectivity ( $Z_e$ ) and (d)–(f) maximum diagnosed hail size ( $D_{h,\max}$ ) in the convective core regions for the (left) 2-MOM\_DLIM, (center) 2-MOM, and (right) 3-MOM 250-m simulations at approximate 1 km AGL at 55 min. The contour lines in the bottom panels are  $Z_e$  isopleths of 10, 30, and 50 dBZ.

distribution ( $\mu = 0$ ) for mean sizes larger than  $\sim 200 \mu\text{m}$  which can lead to excessive size sorting in two-moment schemes (e.g., Wacker and Seifert 2000; MY05a). This relation was based on observations of mainly unrimed ice crystals in midlatitude cirrus and the anvils or stratiform regions of tropical convective systems (Heymsfield 2003) and thus may not be appropriate for heavily rimed ice. The three-moment approach provides an effective and physically based way to control size sorting, but with the extra computational cost of an additional prognostic variable. An alternative to allow the simulation of large ice in the two-moment configuration while controlling size sorting would be to use a different diagnostic- $\mu$  relation, one that tends toward narrowing PSDs (increasing  $\mu$ ) with increasing mean sizes for rimed particles. MY05a and Milbrandt and Yau (2006b) explored the feasibility of this approach and showed that it is possible to reproduce many aspects of a full three-moment scheme with a two-moment hail category that has a diagnostic- $\mu$  designed to control size sorting.

The feasibility of this approach in P3 was examined. We inspected the output from the 3-MOM supercell simulations for  $\mu_i$  and bulk physical properties ( $D_m$  and  $\rho_i$ ), all computed from the prognostic variables, and explored the possibility of deriving a new diagnostic relation. A considerable amount of scatter (not shown) was found. This is not particularly surprising since any derived bulk property comes from a population of ice particles that has 5 degrees of freedom. For two-moment ice in P3, there are 4 degrees of freedom, which is still in stark

contrast with 2 degrees of freedom in the two-moment hail category configuration of MY05a,b.

Nevertheless, we tested a new diagnostic- $\mu_i$  relation, derived mainly from physical reasoning (e.g., large, dense ice [high-density graupel/hail] is more likely to have a narrower PSD due mainly to size sorting; unrimed ice is likely to have wider PSD due to aggregation, breakup, and mixing), some broad guidance from output of the 3-MOM simulation, and trial and error. The following diagnostic relation was tested:

$$\begin{aligned} \mu_i &= 6 \left( 1 - \frac{D_m}{D_{\text{thrs}}} \right), \quad \text{for } D_m < D_{\text{thrs}}, \quad \text{or} \\ \mu_i &= \max[1, 1 + 0.0842(\rho_i - 400)](D_m - D_{\text{thrs}}) \\ &\quad \times F_{\text{rim}}, \quad \text{for } D_m > D_{\text{thrs}} \end{aligned} \quad (13)$$

(in mks units), where  $D_m$  is the mean-mass diameter and  $D_{\text{thrs}} = 0.2 \text{ mm}$ , and a maximum  $\mu_i$  value of 20 is imposed. Essentially (13) reverts to a simplified version of (2) for small ice particles (smaller than 0.2 mm). For larger particles  $\mu_i$  increases linearly with increasing  $D_m$ , with a slope that is proportional to  $\rho_i$ ; the  $F_{\text{rim}}$  factor reduces the value  $\mu_i$  for lower degrees of riming, tending the PSD toward inverse-exponential for completely unrimed ice.

Results from the two-moment simulation using (13) and the relaxed mean size limiter are shown in Fig. 11. The new 2-MOM\_DIAGMU simulation is closer in most respects to 3-MOM than either 2-MOM\_DLIM or 2-MOM. Thus, the two-moment-ice configuration of P3 could, in principle, be

## 2-MOM\_DIAGMU

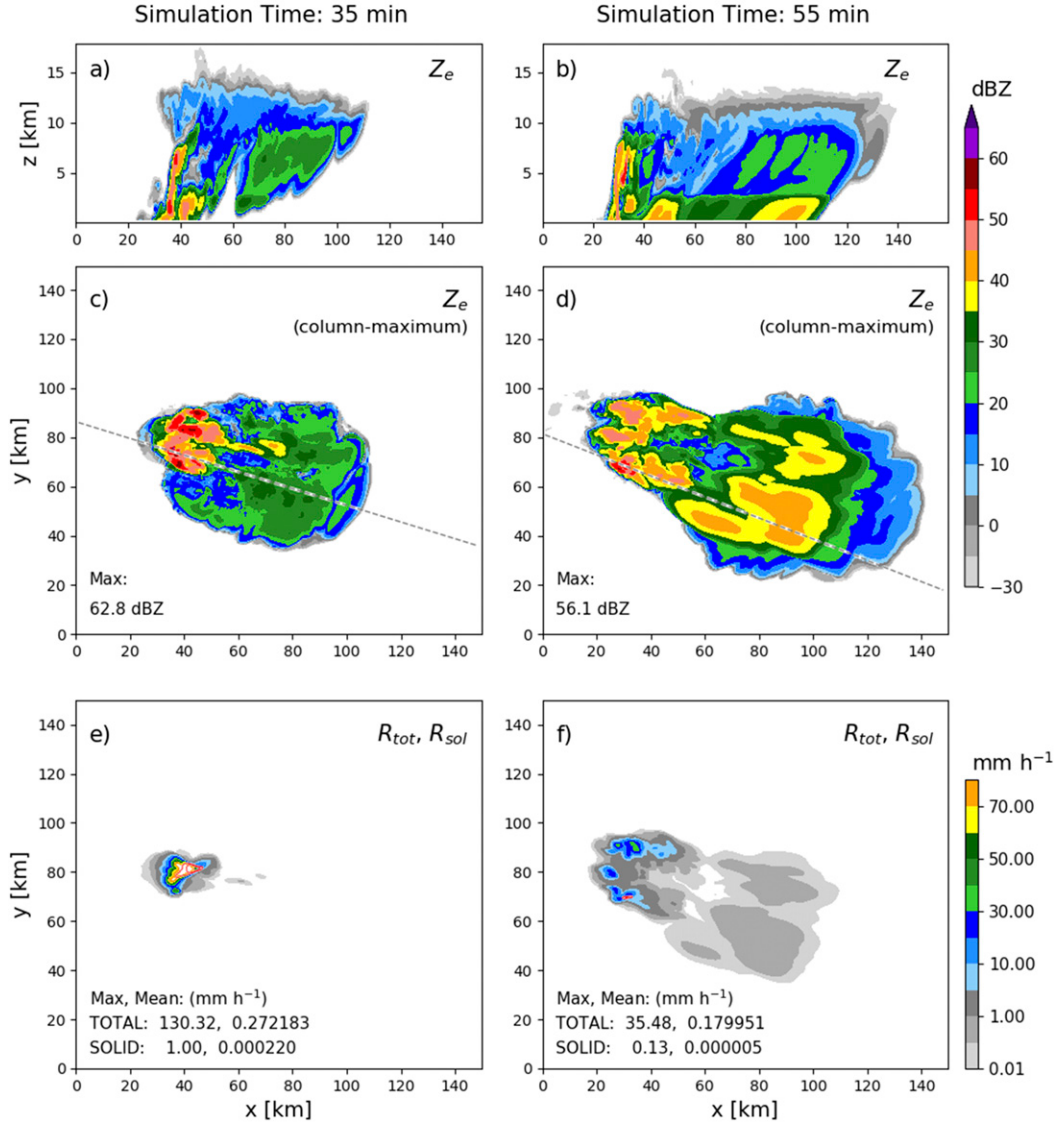


FIG. 11. As in Fig. 7, but for 2-MOM\_DIAGMU at (a),(c),(e) 35 and (b),(d),(f) 55 min.

improved in general through alternative diagnostic- $\mu_i$  relations. However, the test of this new relation was for a single case and for one type of storm, which was dominated by riming growth of ice. The relation given by (13) would need to be tested in a wider range of conditions, and likely modified, to establish general validity. The test described above is presented as a proof of concept for potential further examination and improvement to the two-moment ice configuration.

We argue, however, that the three-moment ice approach in P3 (and microphysics schemes in general) is preferable overall. The computational cost of advection (etc.) for one additional hydrometeor scalar (plus the marginal additional cost in the scheme itself) is becoming less and less important due to improved numerical methods for advection in dynamical models and to increasing computer power. In research mode, the extra

cost is unlikely to be of practical concern. Moreover, for operational models with semi-Lagrangian advection the cost of an additional scalar is marginal. For models using Eulerian advection (e.g., WRF), the P3 scheme lends itself very well to the application of the *scaled flux vector transport* method (Morrison et al. 2016), in which the cost of advection of groups of related prognostic variables (e.g., those for a hydrometeor category) is dominated by a single lead variable (e.g.,  $Q_{i\_tot}$ ), with only marginal additional cost for the advection of the related “secondary” variables (e.g.,  $Q_{i\_rim}$ ,  $N_{i\_tot}$ ,  $B_{i\_rim}$ ,  $Z_{i\_tot}$ ).

### *b. Impact of the choice of advected three-moment variable*

As indicated in section 2, although  $Z_{i\_tot}$  is the new prognostic variable for the three-moment ice configuration of P3, it

is the quantity  $Z_{\text{advec}}$ , given by (12), that is advected and diffused by the dynamics of the driving model. It is not intuitively obvious why this approach would be taken, but it was shown theoretically in Morrison et al. (2016) and numerically in Paukert et al. (2019) that for three-moment schemes, this approach works better to preserve important diagnostic microphysical quantities during advection, which are all functions of the advected variables. Here, “preserved” means that the diagnosed quantities remain constant during advection if the prognostic variables are initially spatially homogeneous over a region of hydrometeors, as should occur physically and consistent with analytic solutions for linear advection. It turns out that in two-moment (and three-moment) schemes,  $N_0$  and  $\lambda$  (as well as quantities such as  $D_m$ ) are preserved through the advection of the mass and number mixing ratios. However, in three-moment schemes (or interfaces) that use the same prognostic variable (e.g., the sixth moment of the PSD) in the dynamics as in the microphysics scheme, as done in Milbrandt and Yau (2006a) and others, this configuration is suboptimal since it does not strictly preserve  $\mu$  and other parameters. By advecting/diffusing  $Z_{\text{advec}}$  instead of  $Z_{i,\text{tot}}$ ,  $\mu$  is a function of the ratio of advected variables ( $Z_{\text{advec}}$  and  $Q_{i,\text{tot}}$ ) and thus is preserved. For details of the specific conditions that must be met in order to preserve bulk quantities during transport, see Morrison et al. (2016).

To test the choice of the new transported variable in P3 (associated with the third prognostic moment), the three-moment simulation discussed in the previous section was rerun but with  $Z_{i,\text{tot}}$  as the prognostic variable passed to the model dynamics, rather than  $Z_{\text{advec}}$  as in 3-MOM. Figures 12a–e show various diagnostic fields for the simulation using advection of  $Z_{i,\text{tot}}$  (3-MOM\_ADVZ) for direct comparison to the original 3-MOM, with advection of  $Z_{\text{advec}}$  (Fig. 9). We also compare  $Z_e$  (Fig. 12f) to that of the original (Fig. 8c). While the differences are generally small, they are nonnegligible. For example, there is less ice mass at lower elevations under the anvil (e.g., 4 km; Fig. 12a) and correspondingly lower reflectivity values there (Fig. 12f). Although the overall impacts are small, advecting  $Z_{\text{advec}}$  rather than  $Z_{i,\text{tot}}$  is mathematically more consistent and the computational cost differences are negligible. Modelers working with three-moment schemes are therefore advised to follow the criteria in Morrison et al. (2016) for choosing the specific quantity to advect, rather than simply directly passing the prognostic microphysics variables to the model dynamics.

#### c. Comparison to 1-km simulations

A grid spacing of 250 m was chosen for the supercell simulations in this study in order to focus on the effects of changes to the microphysics scheme without the complications of interpreting results that may be affected by poorly resolved dynamics. For comparison (and testing), simulations were also run with 1-km grid spacing, a configuration of high-resolution NWP models to which many operational weather centers are moving. While there is more detail in the 250-m runs, the reflectivity structures in the 1-km simulations (Fig. 13) were qualitatively similar to the corresponding 250-m runs (Fig. 8) using the same P3

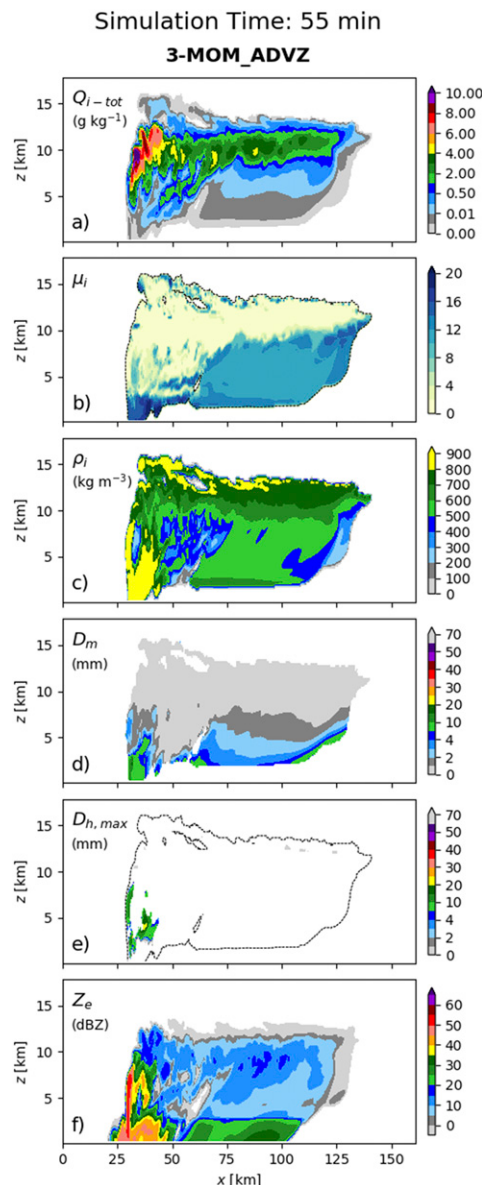


FIG. 12. (a)  $Q_{i,\text{tot}}$ , (b)  $\mu_i$ , (c)  $\rho_i$ , (d)  $D_m$ , (e)  $D_{h,\text{max}}$ , and (f)  $Z_e$  from the 3-MOM\_ADVZ 250-m simulation at 55 min. Dashed contours denote a  $Q_{i,\text{tot}}$  value of  $10^{-3} \text{ g kg}^{-1}$ .

configuration. The total and solid precipitation rates are much higher in 3-MOM at 1 km (Fig. 13i) compared to the two-moment runs, unlike the 250-m run (Fig. 8i), though this appears to be due to the left (northern) storm core being notably more intense for 3-MOM; for the left (southern) core the differences in precipitation are similar for the 1-km runs as the 250-m runs, including hail at the surface in the downshear flank for 2-MOM (Fig. 13h). The 1-km simulations also had similar relative differences in other fields (not shown), such as those in Fig. 9 for the 250-m runs. Hence, the overall conclusions about the impacts of modifying P3, based on the 250-m simulations discussed, are similar for a 1-km setup, at least for this case.

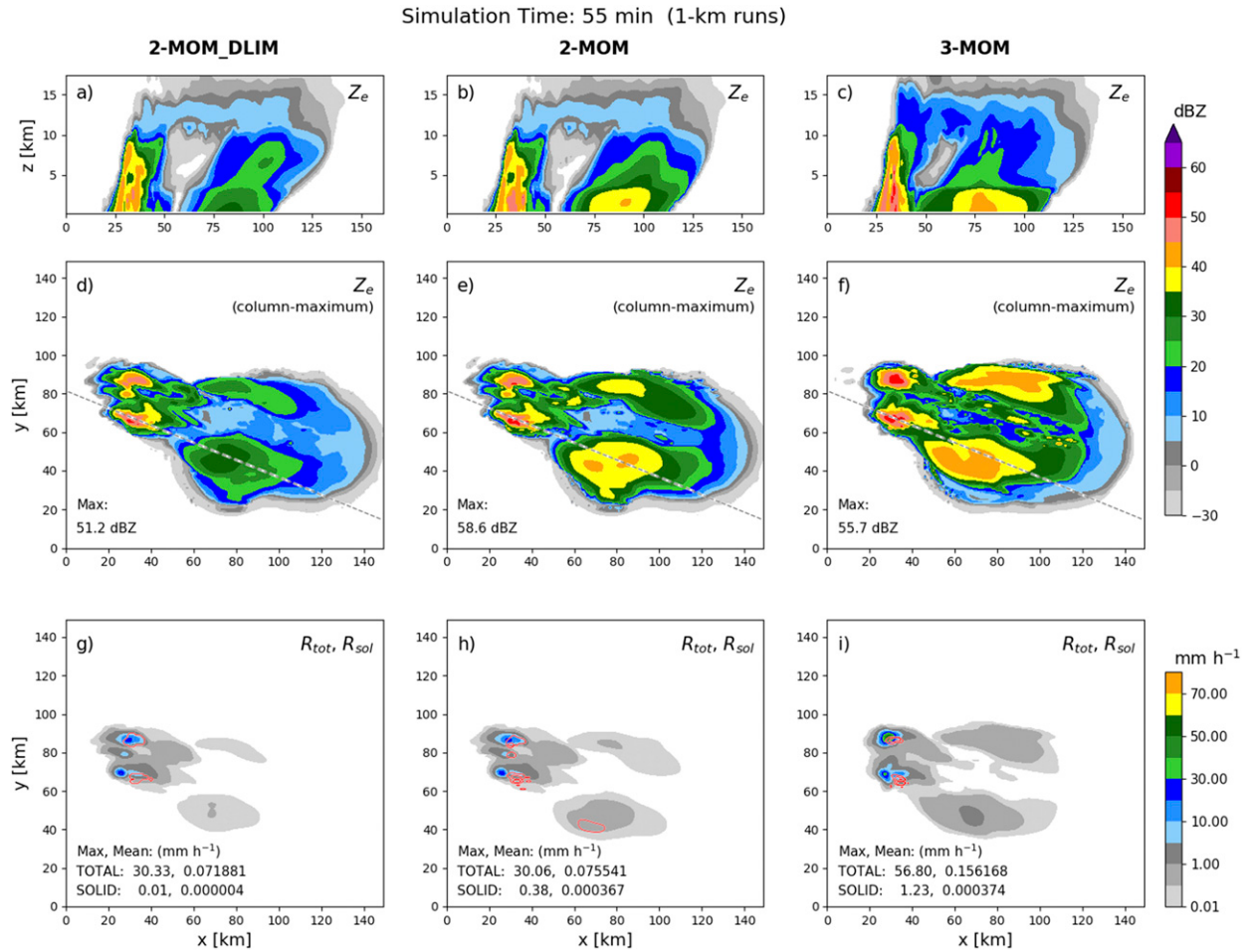


FIG. 13. As in Fig. 8, but for the 1-km simulations.

## 6. Conclusions

The Predicted Particle Properties (P3) bulk microphysics scheme has been modified to allow for an optional triple-moment representation of the ice category(ies). This provides the general benefits of the three-moment approach, which in general means an additional degree of freedom to evolve each ice PSD. This allows the spectral width to vary independently from the other PSD parameters. The three-moment ice development addresses a limitation in the original P3 scheme that did not allow for the prediction of large mean ice particle sizes, which limited its ability to simulate hail. With the three-moment configuration, it is now possible to relax (remove) the imposed limit on the maximum mean ice size in P3 while improving the treatment of sedimentation and thereby properly controlling gravitational size sorting in a physically based way. While details of the three-moment ice scheme were largely based on MY05b, aspects were modified for the specific way that ice is parameterized in P3, which is considerably different than in traditional predefined category-based schemes.

The new three-moment ice P3 scheme, along with two-moment configurations with and without the strict size limiter,

was tested in a simple 1D kinematic model and with near large-eddy-resolving (250-m grid spacing) idealized 3D simulations of a hail-producing supercell. It was shown in both model contexts that whereas the original two-moment scheme indeed produces relatively small mean ice sizes, relaxing the size limiter—but keeping the same diagnostic relation for the ice distribution shape parameter—results in much larger mean sizes and correspondingly higher (unrealistic) reflectivity values due to uncontrolled size sorting. The three-moment ice scheme produces narrower ice size distributions at lower altitudes and thus controls size sorting while still allowing large mean sizes and larger, more realistic, peak reflectivity values. The overall simulation of hail appears to be the most realistic with the three-moment ice configuration. Future work will involve examining the effects on simulated polarimetric fields to confirm that the three-moment configuration does indeed lead to notable improvements compared to what was reported in Johnson et al. (2019) for the original two-moment version of P3 (with two ice categories).

This study has been framed in the context of improving the simulation of hail in P3 and indeed the simulation of hail in a bulk microphysics scheme is best done with the

three-moment method (Milbrandt and Yau 2006b; Dawson et al. 2014; Loftus et al. 2014). This modification to P3 thus represents a significant advancement to that end. However, other aspects that are important for the overall proper representation of hail include predicting the liquid fraction of the mixed-phase ice particles in order to better model wet growth of hail and melting. At time of this writing, the predicted liquid fraction version of P3 (Cholette et al. 2019) is being merged with the three-moment ice version presented here. Future work will examine the effect of this combination on the simulation of hail growth and melting. The three-moment rain component of P3, described in Paukert et al. (2019), will also eventually be merged. Other processes that affect the spectral dispersion of the distributions of unrimed ice, such as aggregation and breakup, will be examined in the future.

This study was also restricted to the single-ice category configuration of P3. At high resolution (subkilometer grid spacing), the particle property dilution problem very likely causes a reduction in the simulated hail sizes with the single-ice P3, since hail-like ice falling through the main updraft will mix and thus merge with smaller ice being transported upward from below, thereby reducing the mean and maximum sizes of the ice that reaches the surface. Preliminary simulations of the 1 June 2008 supercell with the two-ice-category configuration (i.e., nCat = 2; not shown) do indeed indicate that this has an impact. The full effects of increasing the number of ice categories for the simulation of hail with P3 will also be examined in a future study.

**Acknowledgments.** We appreciate the thorough reviews and constructive comments of Adrian Loftus and the anonymous reviewers.

## APPENDIX

### Diagnosing Maximum Hail Sizes from a Bulk Scheme

Predicting the spectral dispersion means, in principle, better simulation of the concentration of large particles, i.e., the tail of the PSD. Milbrandt and Yau (2006a) illustrated that despite the use of a complete gamma distribution (which mathematically extends from particles of sizes zero to infinity) in a bulk scheme, with the three-moment treatment for hail it is possible to make a reasonable estimate of the maximum particle size that is physically observable. The approach is to compute the flux of hail of a given size  $D^*$  given by

$$R(D^*) = \int_{D^*}^{\infty} V(D)N(D) dD, \quad (\text{A1})$$

where  $V(D)$  is the terminal fall speed of a hailstone of diameter  $D$ , and consider if this flux is physically observable or not. For example, consider that for a given hail size distribution at the surface, for  $D^* = 2\text{ cm}$  there is a flux of  $0.05\text{ m}^{-2}\text{s}^{-1}$ , which is equivalent to 4 hailstones of  $D > 2\text{ cm}$  falling over an area  $20\text{ m}^2\text{ min}^{-1}$ ; this is physically observable. In contrast, for the same size distribution the flux for  $D^* = 3\text{ cm}$  is  $2.3 \times 10^{-4}\text{ m}^{-2}\text{s}^{-1}$ , which is equivalent to 1.4 hailstones over an area

of  $100\text{ m}^2\text{ min}^{-1}$ ; this is likely not observable. The largest size for which the flux given by (A1) is considered physically observable, not just nonzero due to the use of a complete gamma distribution, can be considered to be the maximum hail size. Milbrandt and Yau (2006a) proposed a critical flux value of  $10^{-3}\text{ m}^{-2}\text{s}^{-1}$  to delineate between observable and unobservable. Of course, there is considerable subjectivity in the choice of flux threshold, but this technique provides a potentially useful estimate of the maximum hail size and is more meaningful than simply using the mean diameter. This is particularly true for a scheme with a variable shape parameter, where PSDs with the same mean size can have different dispersions and thus different concentrations of particles with  $D > D^*$  (see Fig. 1).

Alternatively, one could estimate the maximum size by simply considering the number concentration of particles larger than a given size  $D^*$  the incomplete integral of  $N(D)$  from  $D^*$  to infinity (Fig. 1), and defining a threshold concentration. This is similar to the flux method; however, a threshold number concentration to delineate between observable and numerical artifact is less physically intuitive for an observer than a threshold flux.

In the simulations presented, the maximum simulated hail sizes are computed as one means of comparing the effects of the different P3 configurations. The flux method, with a critical threshold of  $1.7 \times 10^{-4}\text{ m}^{-2}\text{s}^{-1}$  is used to determine  $D_{h,\max}$  diagnostically for ice with a bulk density exceeding  $750\text{ kg m}^{-3}$  and rime mass fraction exceeding 0.75, which we define to be hail.

## REFERENCES

- Bryan, G. H., and H. Morrison, 2012: Sensitivity of a simulated squall line to horizontal resolution and parameterization of microphysics. *Mon. Wea. Rev.*, **140**, 202–225, <https://doi.org/10.1175/MWR-D-11-00046.1>.
- , J. C. Wyngaard, and J. M. Fritsch, 2003: Resolution requirements for the simulation of deep moist convection. *Mon. Wea. Rev.*, **131**, 2394–2416, [https://doi.org/10.1175/1520-0493\(2003\)131<2394:RRFTSO>2.0.CO;2](https://doi.org/10.1175/1520-0493(2003)131<2394:RRFTSO>2.0.CO;2).
- Chen, J.-P., and T.-C. Tsai, 2016: Triple-moment modal parameterization for the adaptive growth habit of pristine ice crystals. *J. Atmos. Sci.*, **73**, 2105–2122, <https://doi.org/10.1175/JAS-D-15-0220.1>.
- Cholette, M., H. Morrison, J. A. Milbrandt, and J. M. Theriault, 2019: Parameterization of the bulk liquid fraction on mixed-phase particles in the predicted particle properties (P3) scheme: Description and idealized simulations. *J. Atmos. Sci.*, **76**, 561–582, <https://doi.org/10.1175/JAS-D-18-0278.1>.
- Chosson, F., P. A. Vaillancourt, J. A. Milbrandt, M. K. Yau, and Z. Zadra, 2014: Adapting two-moment microphysics schemes across model resolutions: Subgrid cloud and precipitation fraction and microphysical sub-time step. *J. Atmos. Sci.*, **71**, 2635–2653, <https://doi.org/10.1175/JAS-D-13-0367.1>.
- Dawson, D. T., II, M. Xue, J. A. Milbrandt, and M. K. Yau, 2010: Comparison of evaporation and cold pool development between single-moment and multimoment bulk microphysics schemes in idealized simulations of tornadic thunderstorms. *Mon. Wea. Rev.*, **138**, 1152–1171, <https://doi.org/10.1175/2009MWR2956.1>.

- , E. R. Mansell, Y. Jung, L. J. Wicker, M. R. Kumjian, and M. Xue, 2014: Low-level  $Z_{DR}$  signatures in supercell forward flanks: The role of size sorting and melting of hail. *J. Atmos. Sci.*, **71**, 276–299, <https://doi.org/10.1175/JAS-D-13-0118.1>.
- , M. Xue, J. A. Milbrandt, and A. Shapiro, 2015: Sensitivity of real-data simulations of the 3 May 1999 Oklahoma City tornadic supercell and associated tornadoes to multimoment microphysics. Part I: Storm- and tornado-scale numerical forecasts. *Mon. Wea. Rev.*, **143**, 2241–2265, <https://doi.org/10.1175/MWR-D-14-00279.1>.
- , —, A. Shapiro, J. A. Milbrandt, and A. D. Schenkman, 2016: Sensitivity of real-data simulations of the 3 May 1999 Oklahoma City tornadic supercell and associated tornadoes to multimoment microphysics. Part II: Analysis of buoyancy and dynamic pressure forces in simulated tornado-like vortices. *J. Atmos. Sci.*, **73**, 1039–1061, <https://doi.org/10.1175/JAS-D-15-0114.1>.
- Ferrier, B. S., 1994: A two-moment multiple-phase four-class bulk ice scheme. Part I: Description. *J. Atmos. Sci.*, **51**, 249–280, [https://doi.org/10.1175/1520-0469\(1994\)051<0249:ADMMPF>2.0.CO;2](https://doi.org/10.1175/1520-0469(1994)051<0249:ADMMPF>2.0.CO;2).
- Harrington, J. Y., K. Sulia, and H. Morrison, 2013: A method for adaptive habit prediction in bulk microphysical models. Part I: Theoretical development. *J. Atmos. Sci.*, **70**, 349–364, <https://doi.org/10.1175/JAS-D-12-040.1>.
- Heymsfield, A. J., 2003: Properties of tropical and midlatitude ice cloud particle ensembles. Part II: Applications for mesoscale and climate models. *J. Atmos. Sci.*, **60**, 2592–2611, [https://doi.org/10.1175/1520-0469\(2003\)060<2592:POTAMI>2.0.CO;2](https://doi.org/10.1175/1520-0469(2003)060<2592:POTAMI>2.0.CO;2).
- Jensen, A., J. Harrington, H. Morrison, and J. A. Milbrandt, 2017: Predicting ice shape evolution in a bulk microphysics model. *J. Atmos. Sci.*, **74**, 2081–2104, <https://doi.org/10.1175/JAS-D-16-0350.1>.
- Johnson, M., Y. Sun, J. A. Milbrandt, H. Morrison, and M. Xue, 2019: Effects of the representation of rimed ice in bulk microphysics schemes on polarimetric signatures. *Mon. Wea. Rev.*, **147**, 3785–3810, <https://doi.org/10.1175/MWR-D-18-0398.1>.
- Jung, Y., M. Xue, and M. Tong, 2012: Ensemble Kalman filter analyses of the 29–30 May 2004 Oklahoma tornadic thunderstorm using one- and two-moment bulk microphysics schemes, with verification against polarimetric radar data. *Mon. Wea. Rev.*, **140**, 1457–1475, <https://doi.org/10.1175/MWR-D-11-00032.1>.
- Kumjian, M., A. V. Ryzhkov, V. M. Melnikov, and T. J. Schuur, 2010: Rapid-scan super-resolution observations of a cyclic supercell with a dual-polarization WSR-88D. *Mon. Wea. Rev.*, **138**, 3762–3786, <https://doi.org/10.1175/2010MWR322.1>.
- Lebo, Z. J., and H. Morrison, 2015: Effects of horizontal and vertical grid spacing on mixing in simulated squall lines and implications for convective strength and structure. *Mon. Wea. Rev.*, **143**, 4355–4375, <https://doi.org/10.1175/MWR-D-15-0154.1>.
- Lemon, L., and C. A. Doswell III, 1979: Severe thunderstorm evolution and mesocyclone structure as related to tornado genesis. *Mon. Wea. Rev.*, **107**, 1184–1197, [https://doi.org/10.1175/1520-0493\(1979\)107<1184:STEAMS>2.0.CO;2](https://doi.org/10.1175/1520-0493(1979)107<1184:STEAMS>2.0.CO;2).
- Lim, K.-S., and S.-Y. Hong, 2010: Development of an effective double-moment cloud microphysics scheme with prognostic cloud condensation nuclei (CCN) for weather and climate models. *Mon. Wea. Rev.*, **138**, 1587–1612, <https://doi.org/10.1175/2009MWR2968.1>.
- Loftus, A. M., W. R. Cotton, and G. G. Carrio, 2014: A triple-moment hail bulk microphysics scheme. Part I: Description and initial evaluation. *Atmos. Res.*, **149**, 35–57, <https://doi.org/10.1016/j.atmosres.2014.05.013>.
- Mansell, E. R., 2010: On sedimentation and advection in multimoment bulk microphysics. *J. Atmos. Sci.*, **67**, 3084–3094, <https://doi.org/10.1175/2010JAS3341.1>.
- Meyers, M. P., R. L. Walko, J. Y. Harrington, and W. R. Cotton, 1997: New RAMS cloud microphysics parameterization. Part II: The two-moment scheme. *Atmos. Res.*, **45**, 3–39, [https://doi.org/10.1016/S0169-8095\(97\)00018-5](https://doi.org/10.1016/S0169-8095(97)00018-5).
- Milbrandt, J. A., and M. K. Yau, 2005a: A multimoment bulk microphysics parameterization. Part I: Analysis of the role of the spectral shape parameter. *J. Atmos. Sci.*, **62**, 3051–3064, <https://doi.org/10.1175/JAS3534.1>.
- , and —, 2005b: A multimoment bulk microphysics parameterization. Part II: A proposed three-moment closure and scheme description. *J. Atmos. Sci.*, **62**, 3065–3081, <https://doi.org/10.1175/JAS3535.1>.
- , and —, 2006a: A multimoment bulk microphysics parameterization. Part III: Control simulation of a hailstorm. *J. Atmos. Sci.*, **63**, 3114–3136, <https://doi.org/10.1175/JAS3816.1>.
- , and —, 2006b: A multimoment bulk microphysics parameterization. Part IV: Sensitivity experiments. *J. Atmos. Sci.*, **63**, 3137–3159, <https://doi.org/10.1175/JAS3817.1>.
- , and R. McTaggart Cowan, 2010: Sedimentation error in bulk microphysics schemes. *J. Atmos. Sci.*, **67**, 3931–3948, <https://doi.org/10.1175/2010JAS3541.1>.
- , and H. Morrison, 2016: Parameterization of cloud microphysics based on the prediction of bulk ice particle properties. Part III: Introduction of multiple free categories. *J. Atmos. Sci.*, **73**, 975–995, <https://doi.org/10.1175/JAS-D-15-0204.1>.
- , J. Thériault, and R. Mo, 2014: Modeling the phase transition associated with melting snow in a 1D kinematic framework: Sensitivity to the microphysics. *J. Pure Appl. Geophys.*, **171**, 303–322, <https://doi.org/10.1007/s0024-012-0552-y>.
- Morrison, H., and W. W. Grabowski, 2008: A novel approach for representing ice microphysics in models: Description and tests using a kinematic framework. *J. Atmos. Sci.*, **65**, 1528–1548, <https://doi.org/10.1175/2007JAS2491.1>.
- , and J. A. Milbrandt, 2015: Parameterization of ice microphysics based on the prediction of bulk particle properties. Part I: Scheme description and idealized tests. *J. Atmos. Sci.*, **72**, 287–311, <https://doi.org/10.1175/JAS-D-14-0065.1>.
- , G. Thompson, and V. Tatarskii, 2009: Impact of cloud microphysics on the development of trailing stratiform precipitation in a simulated squall line: Comparison of one- and two-moment schemes. *Mon. Wea. Rev.*, **137**, 991–1007, <https://doi.org/10.1175/2008MWR2556.1>.
- , J. A. Milbrandt, G. Bryan, K. Ikeda, S. A. Tessendorf, and G. Thompson, 2015: Parameterization of cloud microphysics based on the prediction of bulk ice particle properties. Part II: Case study comparisons with observations and other schemes. *J. Atmos. Sci.*, **72**, 312–339, <https://doi.org/10.1175/JAS-D-14-0066.1>.
- , A. J. Jensen, J. Y. Harrington, and J. A. Milbrandt, 2016: Advection of coupled hydrometeor quantities in bulk cloud microphysics schemes. *Mon. Wea. Rev.*, **144**, 2809–2829, <https://doi.org/10.1175/MWR-D-15-0368.1>.
- Murakami, M., 1990: Numerical modeling of dynamical and microphysical evolution of an isolated convective cloud—The 19 July 1981 CCOPE cloud. *J. Meteor. Soc. Japan*, **68**, 107–128, [https://doi.org/10.2151/jmsj1965.68.2\\_107](https://doi.org/10.2151/jmsj1965.68.2_107).
- Naylor, J., and M. S. Gilmore, 2012: Convective initiation in an idealized cloud model using an updraft nudging technique.

- Mon. Wea. Rev.*, **140**, 3699–3705, <https://doi.org/10.1175/MWR-D-12-00163.1>.
- Paukert, M., J. Fan, P. J. Rasch, H. Morrison, J. A. Milbrandt, J. Shpund, and A. Khain, 2019: Three-moment representation of rain in a bulk microphysics model. *J. Adv. Model. Earth Syst.*, **11**, 257–277, <https://doi.org/10.1029/2018MS001512>.
- Putnam, B. J., M. Xue, Y. Jung, N. Snook, and G. Zhang, 2014: The analysis and prediction of microphysical states and polarimetric radar variables in a mesoscale convective system using double-moment microphysics, multi-network radar data, and the ensemble Kalman filter. *Mon. Wea. Rev.*, **142**, 141–162, <https://doi.org/10.1175/MWR-D-13-00042.1>.
- , —, —, —, and —, 2019: Ensemble Kalman filter assimilation of polarimetric radar observations for the 20 May 2013 Oklahoma tornadic supercell case. *Mon. Wea. Rev.*, **147**, 2511–2533, <https://doi.org/10.1175/MWR-D-18-0251.1>.
- Reisner, J., R. M. Rasmussen, and T. Bruintjes, 1998: Explicit forecasting of supercooled liquid water in winter storms using the MM5 mesoscale model. *Quart. J. Roy. Meteor. Soc.*, **124**, 1071–1107, <https://doi.org/10.1002/qj.49712454804>.
- Rogers, R. R., and M. K. Yau, 1989: *A Short Course in Cloud Physics*. Pergamon, 293 pp.
- Seifert, A., and K. D. Beheng, 2006: A two-moment cloud microphysics parameterization for mixed-phase clouds. Part I: Model description. *Meteor. Atmos. Phys.*, **92**, 45–66, <https://doi.org/10.1007/s00703-005-0112-4>.
- Shipway, B., and A. Hill, 2012: Diagnosis of systematic differences between multiple parametrizations of warm rain microphysics using a kinematic framework. *Quart. J. Roy. Meteor. Soc.*, **138**, 2196–2211, <https://doi.org/10.1002/qj.1913>.
- Skamarock, W. C., and Coauthors, 2008: A description of the Advanced Research WRF version 3. NCAR Tech. Note NCAR/TN-475+STR, 113 pp., <http://doi.org/10.5065/D68S4MVH>.
- Smith, P. L., 1984: Equivalent radar reflectivity factors for snow and ice particles. *J. Climate Appl. Meteor.*, **23**, 1258–1260, [https://doi.org/10.1175/1520-0450\(1984\)023<1258:ERRFFS>2.0.CO;2](https://doi.org/10.1175/1520-0450(1984)023<1258:ERRFFS>2.0.CO;2).
- Sulia, K. J., H. Morrison, and J. Y. Harrington, 2014: Dynamical and microphysical evolution during mixed-phase cloud glaciation simulated using the bulk adaptive habit prediction model. *J. Atmos. Sci.*, **71**, 4158–4180, <https://doi.org/10.1175/JAS-D-14-0070.1>.
- Thompson, G., and T. Eidhammer, 2014: A study of aerosol impacts on clouds and precipitation development in a large winter cyclone. *J. Atmos. Sci.*, **71**, 3636–3658, <https://doi.org/10.1175/JAS-D-13-0305.1>.
- Tsai, T.-C., and J.-P. Chen, 2020: Multimoment ice bulk microphysics scheme with consideration for particle shape and apparent density. Part I: Methodology and idealized simulation. *J. Atmos. Sci.*, **77**, 1821–1850, <https://doi.org/10.1175/JAS-D-19-0125.1>.
- Wacker, U., and A. Seifert, 2000: On shock-type solutions for the precipitation concentration in models with parameterized microphysics. *Proc. 13th Int. Conf. on Clouds and Precipitation*, Reno, NV, ICCP, 580–583.
- Wang, H., W. C. Skamarock, and G. Feingold, 2009: Evaluation of scalar advection schemes in the advanced research WRF Model using large-eddy simulations of aerosol–cloud interactions. *Mon. Wea. Rev.*, **137**, 2547–2558, <https://doi.org/10.1175/2009MWR2820.1>.
- Xue, M., Y. Jung, and G. Zhang, 2010: State estimation of convective storms with a two-moment microphysics scheme and an ensemble Kalman filter: Experiments with simulated radar data. *Quart. J. Roy. Meteor. Soc.*, **136**, 685–700, <https://doi.org/10.1002/qj.593>.
- Yang, J., and M. K. Yau, 2008: A new triple-moment blowing snow model. *Bound.-Layer Meteor.*, **126**, 137–155, <https://doi.org/10.1007/s10546-007-9215-4>.
- Ziegler, C. L., 1985: Retrieval of thermal and microphysical variables in observed convective storms. Part I: Model development and preliminary testing. *J. Atmos. Sci.*, **42**, 1487–1509, [https://doi.org/10.1175/1520-0469\(1985\)042<1487:ROTAMV>2.0.CO;2](https://doi.org/10.1175/1520-0469(1985)042<1487:ROTAMV>2.0.CO;2).